HOKKAIDO UNIVERSITY

Title	One-dimensional modelling of the nozzle cooling with cryogenic oxygen flowing through helical channels in a hybrid rocket
Author(s)	Gallo, Giuseppe; Kamps, Landon; Hirai, Shota et al.
Citation	Acta astronautica, 210, 176-196 https://doi.org/10.1016/j.actaastro.2023.05.013
Issue Date	2023-09
Doc URL	https://hdl.handle.net/2115/94781
Rights	© <2023>. This manuscript version is made available under the CC-BY-NC-ND 4.0 license http://creativecommons.org/licenses/by-nc-nd/4.0/
Rights(URL)	https://creativecommons.org/licenses/by-nc-nd/4.0/
Type	journal article
File Information	Rev1-1-2-2.pdf

Hokkaido University Collection of Scholarly and Academic Papers : HUSCAP

One-Dimensional Modelling of the Nozzle Cooling with Cryogenic Oxygen Flowing through Helical Channels in a Hybrid Rocket

Giuseppe Gallo[1], Landon Kamps[2], Shota Hirai[3], Carmine Carmicino[4], Harunori Nagata[5]

Hokkaido University, Sapporo, Hokkaido, 060-8628, Japan.

Abstract

A one-dimensional model of the cooling process occurring in a hybrid-rocket nozzle working with cryogenic oxygen flowing through helical channels is addressed in this work. Although the regenerative cooling system in rocket engines involves further complexity, it is here investigated as an option for the suppression of graphite-nozzle erosion in hybrid rockets. The model is based on the solution of the conservation equations of mass, momentum, and energy of the coolant. The Modified Benedict-Webb-Rubin equation of state was used for its accuracy in both the fluid phases of oxygen. The conservation equations for the coolant flow are coupled with a one-dimensional heat transfer model for the evaluation of the nozzle wall temperature at both the cold and hot sides, which has allowed assessing the developed model prediction capabilities by means of the data collected from three engine hot firings. Thus, parametric analyses were carried out to show the effect of the number of helical channels and evaluate the performance improvement obtained in supercritical conditions.

[1] JSPS International fellow, Department of Mechanical and Space Engineering, and AIAA Member.

[2] Specially Appointed Assistant Professor, Department of Mechanical and Space Engineering, and AIAA Member.

[3] PhD Student, Department of Mechanical and Space Engineering, and AIAA Member.

[4] Research Consultant, currently Baker Hughes, Via F. Matteucci 2, 50127, Firenze, Italy.

[5] Professor, Department of Mechanical and Space Engineering, and AIAA Member.

Nomenclature

a = speed of sound
A = area, m^2
A_i = liquid/gas interface area, m^2
c^* = characteristic velocity, m/s
c_p = specific heat at constant pressure, J/kg·K
c_v = specific heat at constant volume, J/kg·K
D = inner nozzle diameter, m
D_{ext} = external nozzle diameter, m
D_h = hydraulic diameter, m
e = internal energy, J/kg
f = skin friction coefficient
G = mass flux, $kg/m^2 \cdot s$
H = static enthalpy, J/kg
H_0 = total enthalpy, J/kg
h_g = gas heat transfer coefficient, $W/m^2 \cdot K$
h_c = coolant heat transfer coefficient, $W/m^2 \cdot K$
I = total impulse, Pa
k = thermal conductivity, W/ m·K
l = channel height, m
L = length, m
$\dot{m}$ = mass flow rate, kg/s
M_w = molecular weight, g/mol
N_{ch} = number bubble density, m^{-3}
N_{ch} = channel number
N_p = pitch number
Nu = Nusselt number
OF = mixture ratio
p = pressure, Pa
p_c = chamber pressure, Pa
Δp = pressure jump, Pa
P = channel perimeter, m
Pr = Prantdl number
$\dot{q}$ = heat flux per unit of area, W/m^2
$\dot{Q}$ = heat flux per unit of length, W/ m
$\dot{Q}_{vap}$ = vaporization enthalpy, J/kg
R = ideal gas costant, J/(mol·K)
$\dot{r}$ = regression rate, mm/s
Re = Reynolds number
Re_ε = rough Reynolds number
t = time, s
t_w = nozzle thickness, m
T = temperature, K
T_0 = flame temperature, K
u = velocity, m/s
w = channel/fins width, m
X_v = vapour mass fraction

Greek Symbols

α = swirl angle
α_v = vapour volume fraction
β = accommodation coefficient
ε_w = wall roughness
μ = viscosity, kg/m·s
ρ = density, kg/m^3
η_{c^*} = chamber temperature efficiency
η_{exp} = experimental characteristic velocity efficiency
η_h = experimental to Bartz's heat flux coefficient
η_T = chamber temperature efficiency

Superscripts

$\bar{}$ = time average
$^\circ$ = reference cold properties

Subscripts

a = axial
aw = adiabatic wall
b = burning
c = coolant
ch = channel
exp = experimental
f = fins
g = gas
h = hydraulic
l = liquid
id = ideal
ox = oxidizer
p = pitch
v = vapour
w = wall

1.Introduction

Hybrid rockets have become one of the most studied propulsion systems of the 21st century thanks to the numerous benefits that they can provide. The main distinctive feature of hybrid rockets is the combination of a higher level of safety and simplicity [1, 2]. This has made them popular in the rocketry community, and much advancement is expected in the following years from both the academic and industrial worlds. However, one of the technical challenge to realize the full potential of hybrid rockets is overcoming the issue of nozzle erosion, that is the degradation and the consequent regression of the nozzle inner surface made of a carbon-based insert, which results from the wall chemical reactions occurring with the combustion gas flowing through it [3, 4]. Like solid rocket motors, the thrust chamber of hybrid rockets does not require active cooling because the solid fuel grain acts as a thermal insulating material. Thus, most developers choose not to employ costly and complicated active cooling systems, relying primarily on carbon-based materials for the thermal insulation of the engine sections where the fuel cannot be employed, such as at the nozzle throat. One drawback of carbon-based materials is that the high heat flux typical of the nozzle throat region leads to surface temperatures high enough for thermochemical, or simply "nozzle erosion", to occur.

Nozzle erosion takes place when the temperature of the wall is sufficiently high to facilitate the heterogeneous chemical reactions with the oxidizing species present in the combustion mixture such as H_2O, CO and CO_2. Graphite, as well as other carbon-based materials, which are arguably the most commonly used in hybrid propulsion applications, at high temperatures are extremely sensitive to such an oxidation process [5, 6]. With no cooling, the nozzle throat tends to heat up early into the burn, so that chemical reactions are substantially boosted and the resulting wall erosion occurs typically with rate in the range of 0.01 mm/s to 0.1 mm/s.

From what mentioned so far, nozzle erosion is mainly dependent upon, first, the employed oxidizer and, second, on the temperature field across the nozzle; while the former is usually fixed by the specific impulse, mass, and volume required by the given mission, the latter could be mitigated by means of a cooling system, which lowers the temperatures under the activation value of the erosion reactions – likely to fall between 1500 K and 2000 K [7, 8].

Hybrid rocket developers have historically avoided the use of regenerative cooling as a potential thermal management technique for the nozzle because of the additional complexity arising from the overall system and the poor coolant performance of the oxidizers. Nonetheless, a literature review revealed the existence of numerous reports which conclude that, although not necessarily advantageous in the liquid rocket configuration, oxidizers are feasible coolants. One of those reports is the interesting study conducted by Price [9], who successfully managed to cool down a copper (liquid) rocket nozzle throat using liquid oxygen. A similar effort was made by Yuasa et al. [10] with the further target of vaporizing the liquid oxygen upstream of the injection in a hybrid rocket. Another example is a 1U CubeSat-sized hybrid rocket plug nozzle cooled by nitrous oxide [11]. Note that, in all these cases, metallic nozzles with internal coolant paths were used.

In this scenario, a previous experimental campaign has been performed at the laboratory of space systems of the Hokkaido University, in which the authors have preliminarily shown that carbon-based nozzle erosion could be successfully suppressed by an active cooling system based on cryogenic oxygen [12, 13]; in-depth studies are thus deserving further attention. Here, the cooling of a graphite nozzle, rather than a classical metallic nozzle throat (made of materials like copper, steel or similar ones), still remains a novel concept. Simply put, cooling a graphite nozzle throat increases the safety and reliability level of the system because the risk of catastrophic failures, in the case of anomalous overheating, is mitigated down to a risk of minor performance loss resulting from nozzle erosion.

In recent years, many numerical studies have been published about cooling systems in liquid rocket engines employing axial channels with variable cross-section area. Two different approaches are usually adopted to accomplish this task: either quasi-2D models [14, 15, 16], that, on the one side, are reasonably affordable in terms of computational cost but, on the other, are based on semi-empirical correlations, or fully 2D/3D mechanistic models [17, 18, 19], that are computationally onerous but highly reliable, can be used. The choice of the most proper approach basically depends on the specific aim of the analysis. The latter works are, indeed, intended to study detailed phenomena, e.g. vortex shedding and local heat flux enhancement that could occur along the cooling channels, whereas, the former ones can be useful to study the effect of the main design parameters and carry out more general parametric screenings.

The work was aimed at the development of a sophisticated one-dimensional numerical model for the analysis of cooling systems in hybrid rocket engines utilizing cryogenic oxygen which is fed through helical channels. The previous nozzle cooling configuration based on axial channels has, indeed, been revised and modified to a new layout with helical channels. The numerical tool has been validated through a set of experimental data retrieved from the firing tests mentioned above. Since the oxygen thermodynamic properties significantly vary along the cooling channels for the large temperature rise and pressure drop, an accurate and efficient way to determine the pressure-volume-temperature behaviour of the coolant is needed, for which the modified Benedict-Webb-Rubin equation of state (EOS) [20] has been selected.

This paper consists of three main sections. In the first section, the difference between the configurations with axial and helical channels is presented. In the second one, the numerical model adapted to the helical channels is described. The coolant and the heat transfer equations are detailed, and the assessment of the numerical results against the experimental data is provided. Finally, the advantages and drawbacks of employing the coolant in supercritical conditions, and increasing the number of channels are highlighted.

2. Test Cases Description

In this section, the test rig and the hybrid rocket engine configuration are described. Figure 1 shows a simplified diagram of the experimental facility employed for the firing tests. The fuel and the oxidizer employed in the firing tests are high-density polyethylene and oxygen, respectively. A single line is shown in the picture: liquid oxygen is used for the cooling of the graphite exhaust nozzle and then it is injected into the combustion chamber. The cryogenic liquid oxygen is pressurized through the cooling channels by means of a high-pressure helium tank placed upstream of the liquid oxygen reservoir, which maintains the coolant temperature at around 119 K. Oxygen feeding pipe is thermally insulated to mitigate the coolant heating upstream of the nozzle cooling channels' inlet. A nitrogen tank is included in the main line for purging the engine after combustion. The liquid oxygen reservoir is equipped with load cells, which measure the mass loss of the oxidizer during the burning time.

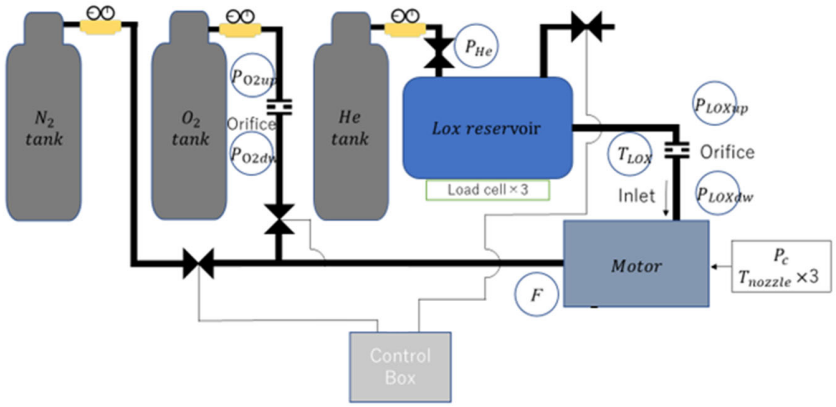

Figure 1 Schematic of the facility used for the experimental tests.

Figure 2 shows a schematic of the engine assembly and the cross section of the fuel grain. The tests presented in the following sections have been performed by injecting oxygen through a large injection chamber, which is part of the dump plenum upstream of the solid fuel grain; the rear portion of the grain has a larger section so that an aft-mixing chamber is set up. Engine ignition is achieved by burning gunpowder; the ignition procedure is not automatic and may vary from test to test.

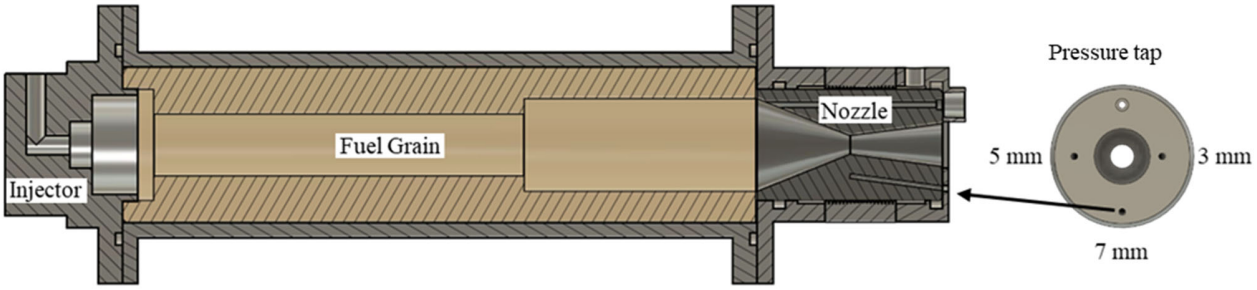

Figure 2 Schematic of the hybrid rocket engine and of the thermocouples position in the nozzle insert.

The exhaust nozzle core is made of graphite; three holes are drilled for inserting K-type thermocouples whose temperature measurement uncertainty is ±5 K. Wall temperature was measured in three radial locations, at 3, 5 and 7 mm far from the inner surface of the throat at three different circumferential positions (see the right side of Figure 2). All the nozzles used in the firing tests were manufactured using the same grade of isotropic graphite (G347; Tokyo Tokai Carbon, Ltd.). The material density and thermal conductivity at room temperature are given by the manufacturer to be $\rho_n = 1850$ kg/m^3 and $k = 116$ W/(m·K), respectively [21]. The temperature dependency of the properties of G347 graphite is not specified by the manufacturer, thus temperature trends have been assumed from previous research on similar high-density graphite [22]. The nozzle length is 60 mm, and the throat is located in the middle. The inlet section to the convergent portion, the throat section and the divergent portion exit section have diameter of 25 mm, 6 mm and 20 mm, respectively. The external diameter (around which the channels are wrapped) is 38 mm. The nozzle is mounted within a metallic case containing three helical fins with equal width and height of 1 mm, travelling around the nozzle axis with a rotation angle of around 3 degrees. Therefore, three helical channels are obtained from the accommodation of the nozzle into the case. The coolant flows in the direction opposite to the one of the exhaust gas. At the outlet of the channels, the heated coolant is gathered in a collector and injected in the main chamber through a pipe. Figure 3 depicts the described assembly, and Figure 4 shows a picture of the exhausted plume of a typical firing test.

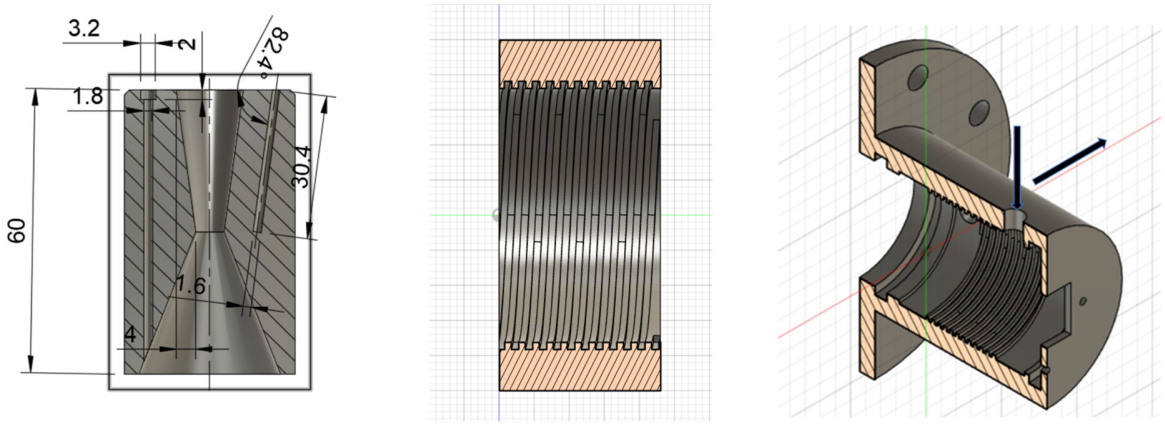

a) Graphite nozzle block. **b) Helical channels.** **c) External case.**

Figure 3 Details of the graphite nozzle assembly.

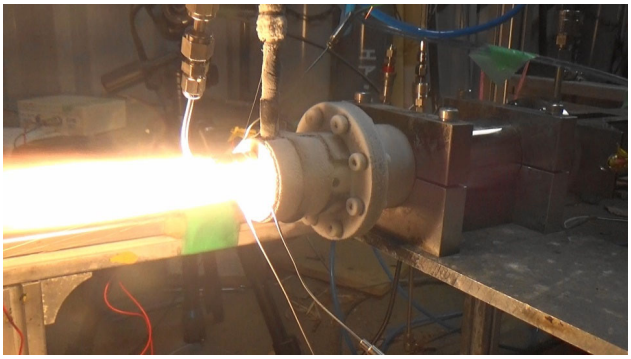

Figure 4 Screenshot of a combustion experiment.

Three firing tests are considered in this work and used as a benchmark for the validation of our numerical model. In all the test cases, no nozzle erosion was detected. The first test, denominated here as Test NC, was performed without active nozzle cooling, while the second and third tests, Test AC1 and AC2, were performed by supplying the coolant with an inlet pressure of around 23 bar. Because the liquid oxygen mostly gasifies in the cooling system in both Test AC1 and Test AC2, in Test NC gaseous oxygen was directly injected into the chamber to provide proper comparison. The oxygen mass flow rate was measured by using a choked orifice placed between the tank and the chamber. Note that, although no erosion was observed in the present firings, a number of other tests performed in a wide range of operating conditions including the ones described in the following, were affected by this phenomenon (for instance, see test *DNT-2 thru -10* of Table 1 in Ref. [7]).

Table 1 summarizes the operating conditions of the three tests. The burning time, t_b, was defined as the time between the pressure rise and fall, corresponding to the engine ignition and shutdown. The time averaged mixture ratio, $\overline{OF}$, was defined by Eq. (1):

$$\overline{OF} = \frac{\bar{\dot{m}}_{ox}}{\bar{\dot{m}}_f} \qquad \bar{\dot{m}}_f = \frac{\Delta \mathrm{M}_f}{t_b} \tag{1}$$

Where $\bar{\dot{m}}_f$ is the time averaged fuel mass flow rate, evaluated as the ratio of the fuel mass consumed, $\Delta \mathrm{M}_f$, and the burning time, t_b. Finally, the characteristic velocity and the corresponding efficiency are defined as:

$$c^*_{exp} = \frac{\bar{p}_c A_t}{\bar{\dot{m}}_f + \bar{\dot{m}}_{ox}}$$
$$\eta_{exp} = \frac{c^*_{exp}}{c^*_{id}} \quad (2)$$

Where the ideal characteristic velocity, c^*_{id}, is evaluated by CEA [23] software by imposing the experimental chamber pressure and mixture ratio.

Table 1. Firing test operating conditions.

Test	$\bar{\dot{m}}_{ox}, g/s$	t_b, s	$\overline{OF}$	$\bar{p}_c, MPa$	$c^*_{exp}, m/s$	η_{exp}
NC	12.4	20	2.48	0.97	1575	0.88
AC1	12.0	20	2.56	0.97	1634	0.92
AC2	12.2	20	2.42	0.98	1606	0.90

Figure 5a shows the pressure signals of Test NC, Test AC1 and Test AC2 over the burning time; pressure slightly increases from around 0.9 to 1.0 MPa. From the picture a fair repeatability of the three firing tests is yielded. Temperatures measured in the nozzle throat section are plotted in Figure 6. Nearly thermal steady state was achieved at the end of the tests equipped with regenerative cooling. The effect of the cooling system on the temperatures can be noticed by comparing the two graphs. For instance, observing the temperature measured at the distance of 3 mm, a maximum temperature of 1000 K was recorded in Test NC and 600 K in Test AC. Therefore, although no nozzle erosion occurred in Test NC, it is likely to occur for longer burning times.

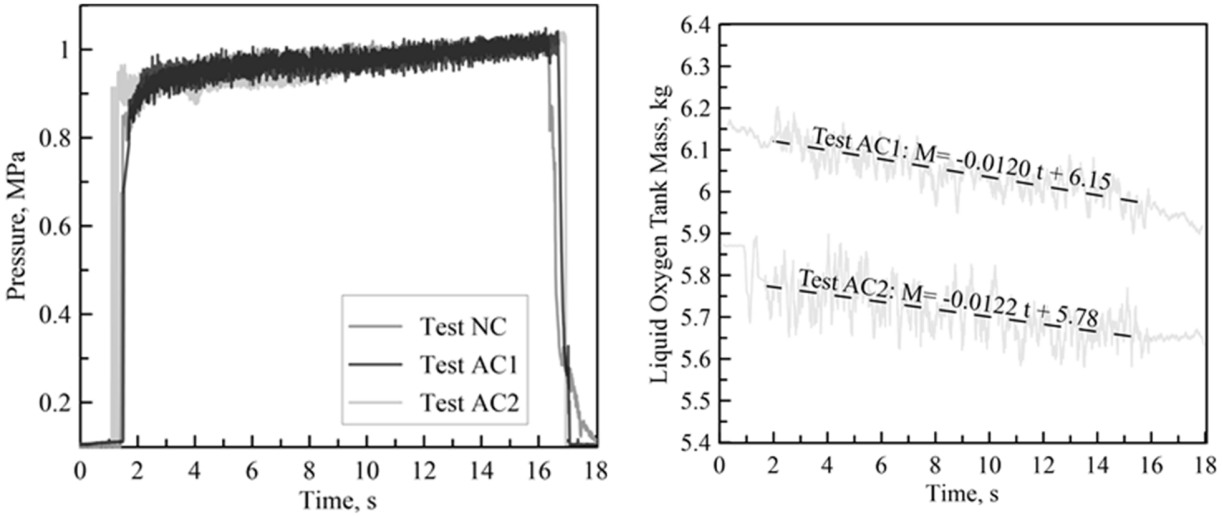

(a) Pressure signals. **(b) Liquid oxygen tank mass.**

Figure 5 Pressure signals and oxygen tank mass during the burning time.

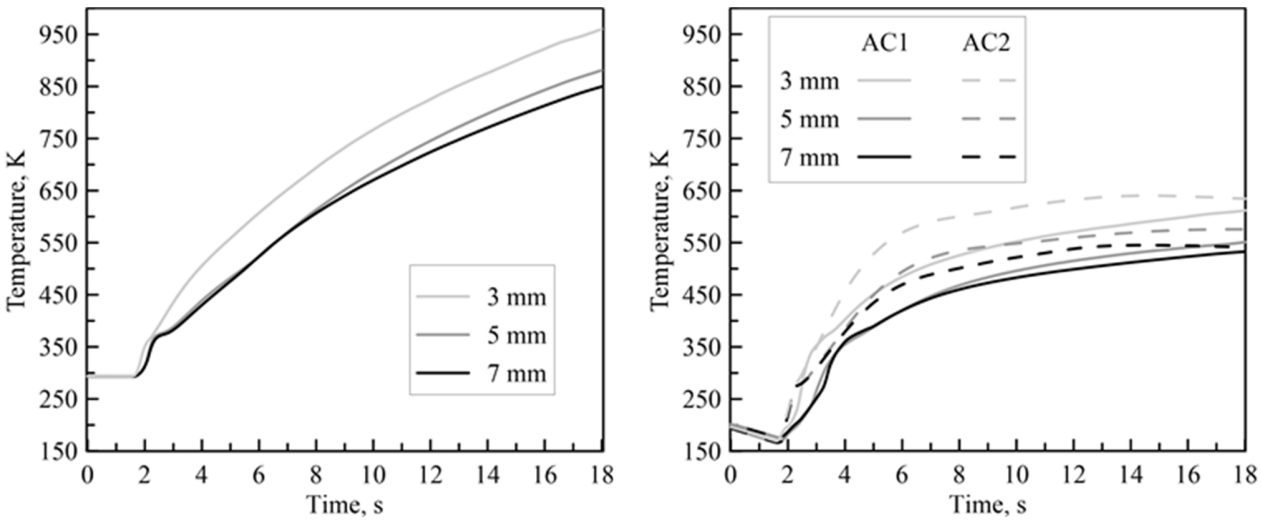

(a) Test NC **(b) Test AC**

Figure 6 Temperature signals measured in the nozzle throat section.

Pressure and temperature recorded in Tests AC2 at the outlet of the helical channels are shown in Figure 7; a pressure drop of around 10 bar and a temperature increase of around 200 K can be seen.

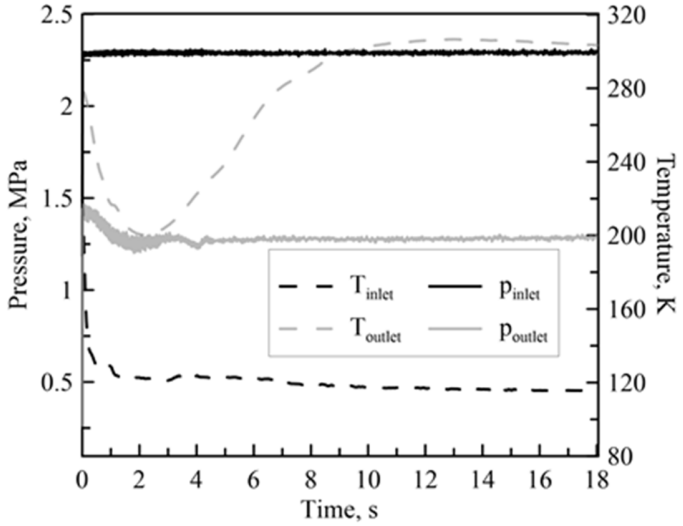

Figure 7 Pressure and temperature at the inlet and outlet of the cooling channels.

3. Cooling System Design Aspects

3.1. Helical Cooling Channel Geometrical Parameters

In this section, the quantities defining the main geometrical parameters involved in the cooling system design are shown and discussed. In Figure 8 a schematic of the cooling channels (which are represented in Figure 3b) is sketched, and the main geometrical parameters appearing in the equations that follow are indicated.

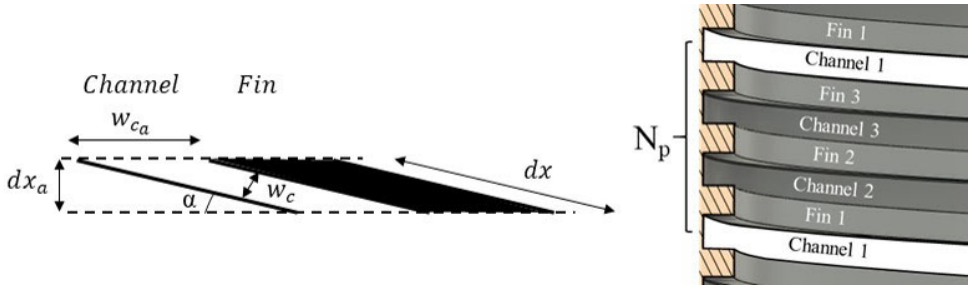

4.Figure 8 Schematic of cooling channels.

The main difference between helical and axial channels is given by the swirl angle, α; note that $\alpha = 90°$ corresponds to the case of axial channels. Once both the nozzle and channel geometry are defined, the swirl angle can be expressed as a function of the number of channels, according to Eq. (3):

$$\alpha = \sin^{-1}\left[\frac{N_{ch}(w_{ch} + w_f)}{\pi D_{ext}}\right] \tag{3}$$

where N_{ch} is the number of channels, w_c and w_f are the width of the channel and of the fin respectively, and D_{ext} is the external diameter. In the present case, the swirl angle is around 3°. Note that, because of the small swirl angle, geometrical quantities normal to the fluid velocity are much lower than their axial projections. For instance, the channel area is 1 mm^2, whereas its axial projection is 20 mm^2 $(1/\sin\alpha \cong 20)$. The helical pitch and channel length are respectively given by:

$$\begin{aligned} L_p &= \frac{N_{ch}(w_{ch} + w_f)}{\cos\ \alpha} \\ L_{ch} &= N_p\sqrt{L_p^2 + \pi D_{ext}^2} \end{aligned} \tag{4}$$

where N_p is the total number of pitches included in the cooling geometry, that is $N_p = L_n/L_p$, and L_n is the nozzle length. The nozzle length being equal to 60 mm, the total channel length is around 1 m. Therefore, the helical channel length is around 17 times the length of the axial channels.

A simplified analysis is developed in the following to show the main differences between the helical and axial channels configurations by varying the number of channels; the results are reported in Figure 9. Figure 9 displays the variation of the swirl angle in the helical configuration with a fixed channel width as a function of the number of channels. α increases from 2 to the maximum value of 90° by correspondingly varying the number of channels from 2 up to 56. The helical configuration coincides with the axial one for $\alpha = 90°$. Figure 9b displays the decreasing trend of the channel width with N_{ch} in the axial configuration from 55 to 1 mm in the same range of N_{ch}.

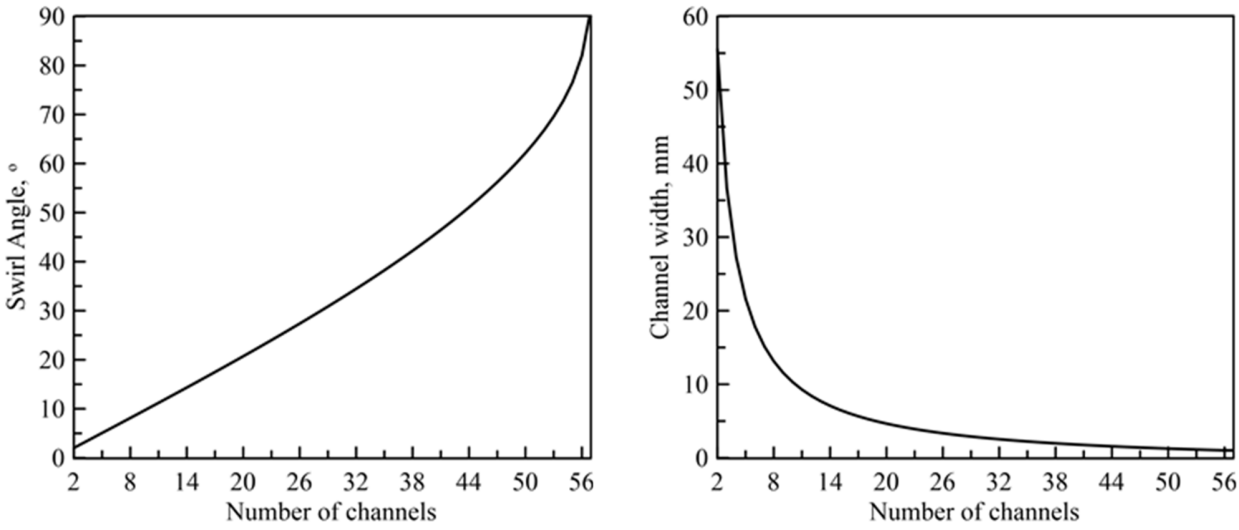

(a) Helical channels. Fixed channel width (1 mm), variable swirl angle.

(b) Axial channels. Variable channel width, fixed swirl angle (90°).

Figure 9 Swirl angle (for helical cooling) and channel width (for axial one) vs number of channels.

To assess the effect of the number of channels on the cooling system capacity, consider the following two classical equations for the pressure drop (Darcy–Weisbach friction factor definition) and convective heat transfer coefficient (Dittus–Boelter equation) in a turbulent flow through a pipe:

$$\Delta p = \frac{1}{2} f \frac{\dot{m}^2}{\rho} \frac{L_{ch}}{A_{ch}^2 D_h}$$
$$Nu = 0.023 Re^{0.8} Pr^{0.4} \tag{5}$$
$$Re = \frac{\dot{m} D_h}{\mu A_{ch}}$$

where f is the friction factor, ρ is the coolant flow density, $\dot{m}$ is the coolant mass flow rate per channel, μ is the coolant dynamic viscosity, Pr is the Prandtl number, D_h is the hydraulic diameter defined as $D_h = 4A_{ch}/P_{ch}$ and P_{ch} is the channel perimeter. In this instance, the thermo-fluid-dynamic quantities are kept constant to the values relative to the cryogenic liquid oxygen in the condition of 23 bar and 120 K (see Table 2). Note that, in the following sections, more accurate relationships are used to estimate both the pressure drop and the convective heat transfer coefficient in the cooling ducts.

Table 2 Thermo-fluid-dynamic properties appearing in Eq. (5).

f	$\rho, kg/m^3$	$\mu, Pa \cdot s$	$\dot{m}, g/s$	Pr
0.01	988	$1 \cdot 10^{-4}$	4	1

Figure 10a displays the pressure drop and Nusselt number in both the axial and helical configurations, both normalized with respect to their corresponding maximum values. In the case of axial channel configuration, both the pressure drop and the Nusselt number increase with the number of channels, because the channel area is reduced. Therefore, the heat transfer is enhanced with the drawback of higher pressure drop. On the other hand, when helical channels are employed, increasing the number of channels results only in a reduction of the axial projection of the channel cross-sectional area, while the cross-

sectional area normal to the fluid velocity remains constant. A counter-intuitive aspect is that the pressure drop decreases with the number of channels because of the shorter channel length, as shown by Eq. (4), with no impacts on the Nusselt number. Figure 10b displays the pressure drop and Nusselt number ratios between helical and axial channels ($\Delta p_{helical}/\Delta p_{axial}$ and $Nu_{helical}/Nu_{axial}$). By comparing the two configurations, the heat transfer in the helical channels is larger than the one in the axial case at the cost of a larger pressure drop. Both those ratios are equal to 1 at the maximum number of channels (56 channels) assumed for the helical case.

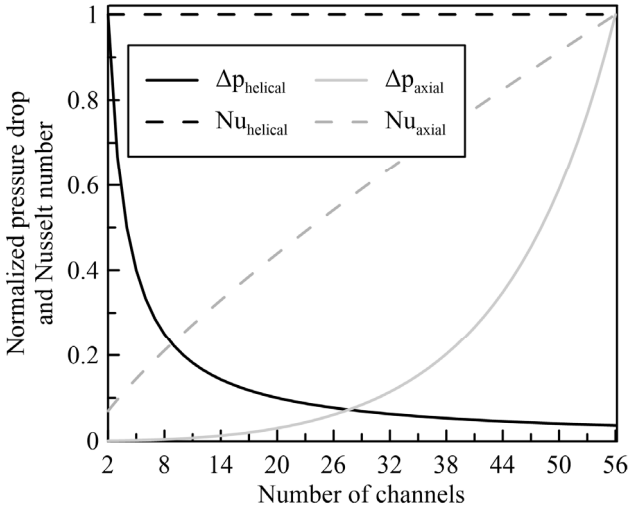

(a) Helical channels. Fixed channel width (1 mm), variable swirl angle.

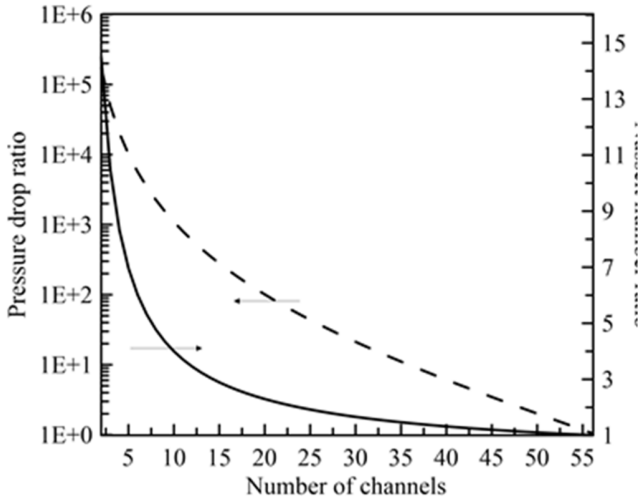

(b) $\Delta p_{helical}/\Delta p_{axial}$ and $Nu_{helical}/Nu_{axial}$.

Figure 10 Pressure drop and Nusselt number ratio in helical and axial channels.

5. Coolant and Heat Transfer Physical and Numerical Model

5.1. Coolant equation of state and thermal properties

The question arises of how fluid behaviour can be described quantitatively. Because of the large number of functions and constants involved in the computation of the coolant properties, all the details have been summarized in Appendix A, where all the information lacking in this section can be found. To represent the thermodynamic state of a fluid, of course a function of the type $F(p,\rho,T)=0$ is needed, which relates pressure, density and temperature. Among all the EOS available in the literature, the authors adopted a correction to the Benedict-Webb-Rubin EOS family, named Modified-Benedict-Webb-Rubin (MBWR) EOS developed by Younglove [24,25]. It is a multiparameter EOS, explicit in pressure. It can be written as:

$$p=\sum_{n=1}^{9}\rho^{n}F_{n-1}+e^{-\delta^{2}}\sum_{n=10}^{15}\rho^{2n-17}F_{n-1} \tag{6}$$

where $\delta=\rho/\rho_c$ and ρ_c is the critical density. The F_{n-1} are functions of the temperature, and they are listed in Appendix A. It is worth noting that the equation above has multiple solutions, especially near the critical point. Therefore, for the correct solution, special attention is required in the choice of the initial guess. The references provided in this work include a computational database, which can be used as a benchmark for readers who are interested in implementing it. Note that, once given Eq. (6), all the thermodynamic properties can be found as a function of two state parameters, in the following pressure, *p,* and temperature *T* [26]. First, the specific enthalpy is determined by means of Eq. (8):

$$H(p,T) = H_{ref}(T_{ref}) + \int_{Tref}^{T} c_{p,0}(T)dT + \frac{p-\rho RT}{\rho} + \int_0^{\rho}\left[\frac{p}{\rho^2} - \frac{T}{\rho^2}\left(\frac{\partial p}{\partial T}\right)_{\rho}\right]_T d\rho \quad (7)$$

where, H_{ref} is the ideal gas reference specific enthalpy at $T_{ref} = 298.15\ K$. The first integral covers the change in specific enthalpy due to an increase in temperature using the ideal gas isobaric specific heat capacity, $c_{p,0}$. The following terms account for the departure from the ideal gas behaviour and they are null in the case of ideal gas. Then, the specific internal energy can be computed from the definition of enthalpy as a function of the specific enthalpy, pressure, and density according to Eq. (8):

$$e(p,T) = H(p,T) + \frac{p}{\rho} \quad (8)$$

The isochoric specific heat capacity can be obtained as the differential of specific internal energy with respect to temperature at constant volume:

$$c_v(p,T) = c_{v,0}(T_{ref}) + \int_0^{\rho}\left[\frac{T}{\rho^2}\left(\frac{\partial^2 p}{\partial T^2}\right)_{\rho}\right]_T d\rho \quad (9)$$

where $c_{v,0}$ is the ideal gas isochoric specific heat capacity. Calculating instead the differential of the specific enthalpy yields the isobaric specific heat capacity:

$$c_p(p,T) = c_v(p,T) + \frac{T}{\rho^2}\frac{\left(\frac{\partial p}{\partial T}\right)_{\rho}^2}{\left(\frac{\partial^2 p}{\partial \rho^2}\right)_T} \quad (10)$$

The speed of sound is calculated with Eq. (11):

$$a^2(p,T) = \frac{c_p(p,T)}{c_v(p,T)} + \frac{T}{\rho^2}\left(\frac{\partial p}{\partial \rho}\right)_T \quad (11)$$

The equations above completely define the thermodynamic state of the coolant. Because of the explicit expression of pressure as function of density and temperature given in Eq. (6), all the derivatives and integrals can be computed analytically. Figure 11 represents the calculated density and specific enthalpy contours. Figure 11a shows the oxygen pT-diagram from the triple point (54.3 K) to the critical point (154.6 K) and above. Remind that the triple point represents the thermodynamic state in which the three phases (solid, liquid and vapour) coexist. Over this point, the phase boundary between liquid and vapour is clearly defined up to the critical point. At extremely high pressures and temperatures, the liquid and gaseous phases become indistinguishable in what is known as the supercritical fluid state. Therefore, three distinct regions can be recognized, which represent the liquid, the gaseous, and the supercritical phases. Figure 11a represents the combination of these three regions. The vapour pressure, P, curve can be easily computed with the following equation:

$$lnP = lnP_t + V_1 x + V_2 x^2 + V_3 x^3 + V_4 x^4 + V_5 x(1-x)^{V_6}$$
$$x = \frac{(1 - T_t/T)}{(1 - T_t/T_c)} \quad (12)$$

where T_c is the critical temperature, and T_t and P_t are the temperature and pressure at the triple point, respectively. Figure 11b represents the specific enthalpy in the same temperature and pressure ranges. Accordingly, the specific enthalpy is still continuous above the critical point and it jumps along the phase curve: this jump physically represents the latent heat of vaporization required for the phase change. Note that this amount of energy depends on the thermodynamic conditions. Again, high vaporization enthalpies are required for phase change far from the critical point.

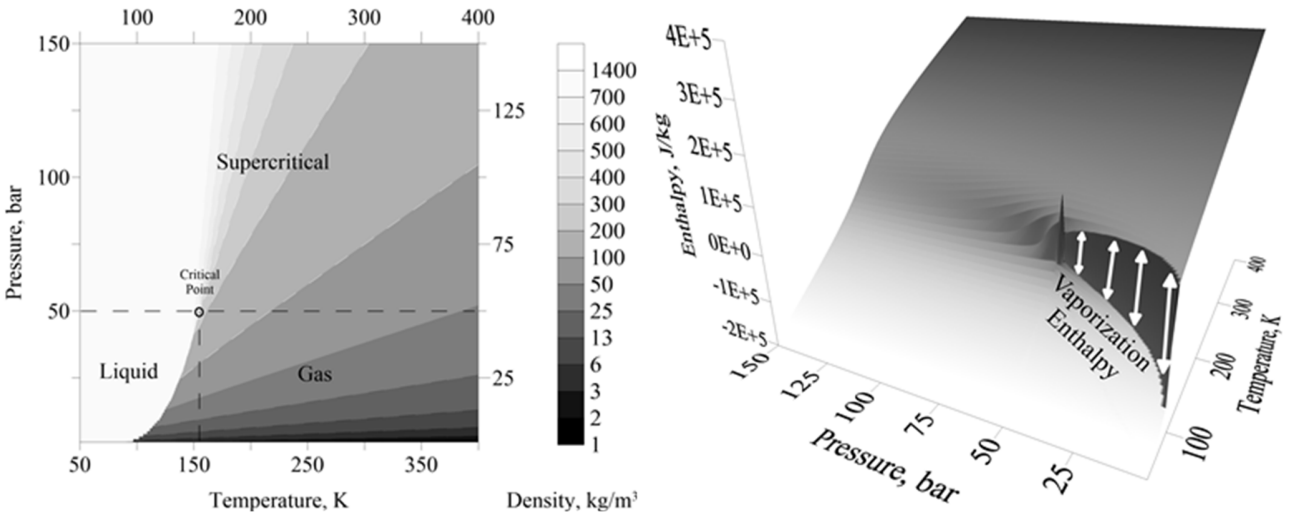

(a) Density. **(b) Sensible specific enthalpy.**

Figure 11. Contours of density and specific enthalpy varying pressure and temperature.

The evaluation of the transport properties (viscosity and thermal conductivity) of a fluid is of great importance to describe its cooling properties. Since the coolant flow is often a high density subcritical/supercritical flow, the rarefied-gas model for transport properties is not accurate; thus, the transport properties are evaluated considering both the contribution of the rarefied-gas term and of the dense-fluid term. The approach employed by Hanley et al. [27] was considered in this work. The viscosity and the thermal conductivity can be written as the sum of three separate contributions:

$$\mu = \mu_0(T) + \mu_1(T)\rho + \mu_2(\rho, T)$$
$$k = k_0(T) + k_1(T)\rho + k_2(\rho, T) + \Delta k_c(\rho, T) \quad (13)$$

where μ_0 and k_0 are the values of the transport coefficient at the temperature in the limit of low pressures, $\mu_{1,2}$ and $k_{1,2}$ are the so-called excess values that measure the enhancement of the viscosity and thermal conductivity, respectively, at a given temperature and density over its dilute gas value, while Δk_c represents the additional anomalous contribution in the region around the critical point.

Figure 12 represents the contours of the computed dynamic viscosity and thermal conductivity. As shown, both the properties are very sensitive to temperature in the liquid phase, while they are approximately constant with pressure. On the other hand, a higher sensitivity to pressure can be observed in the gaseous phase. According to the kinetic theory, they decrease with temperature in the liquid phase because the temperature weakens the intermolecular forces in this phase condition; on the other hand, they increase in the gaseous phase because temperature increases the number of kinetic shocks enhancing the molecular interactions. Similarly to Figure 11, the contours are continuous above the supercritical point and discontinuous below it.

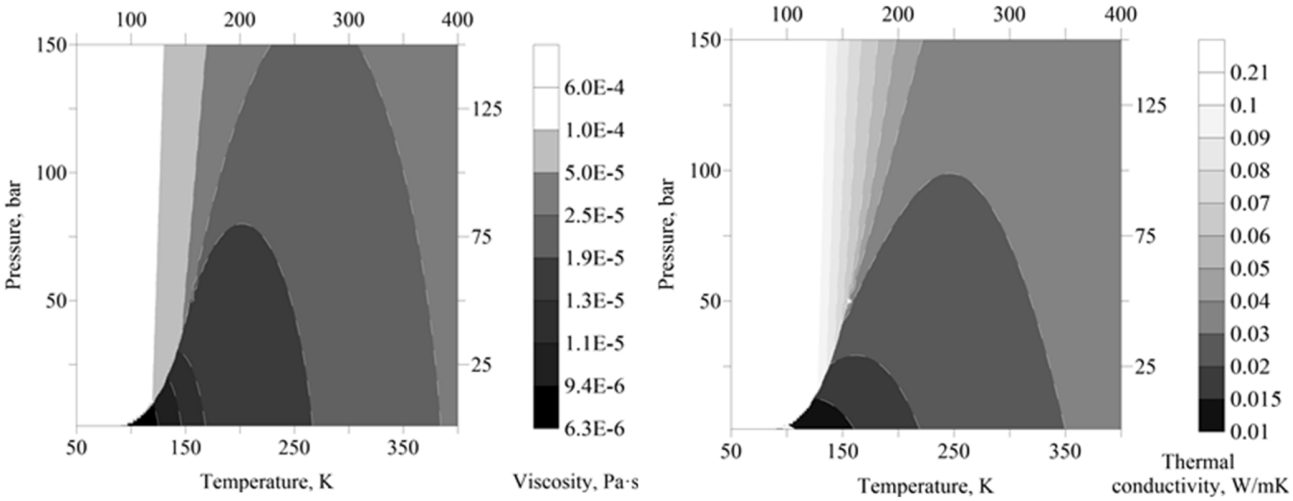

(a) Dynamic viscosity. **(b) Thermal conductivity.**

Figure 12. Contours of the dynamic viscosity and thermal conductivity as functions of pressure and temperature.

5.2.Steady state heat transfer equation

Heat is transferred from the hot gas (subscript g) to the coolant (subscript c) via the solid wall of the graphite nozzle as schematically shown in Figure 13.

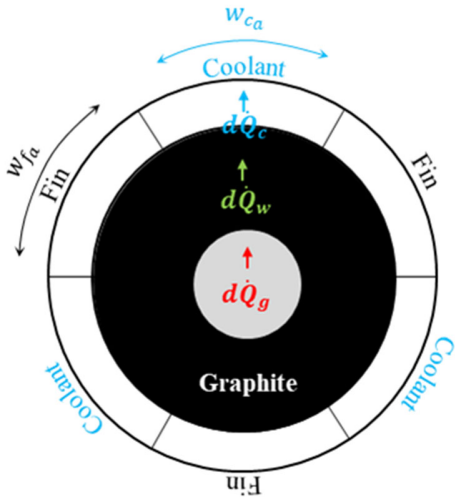

Figure 13 Schematic of heat transfer path from the hot gases to the coolant.

By neglecting the heat transfer along the nozzle axial and circumferential directions, a one-dimensional heat transfer balance between the hot gas, the nozzle wall, and the coolant is considered. Hot-gas exchanges heat by convection to the nozzle wall (the relative heat transfer rate is $d\dot{Q}_g$), which is transmitted by conduction through the wall ($d\dot{Q}_w$), and is transported by convection to the coolant ($d\dot{Q}_c$). In the steady-state conditions, the three heat transfer rates must be equal:

$$d\dot{Q} = d\dot{Q}_g = d\dot{Q}_w = d\dot{Q}_c \tag{14}$$

in which $d\dot{Q}$ is the elemental heat transferred per unit time through the relative nozzle surface. Ignoring the presence of the fins (only the heat transferred to the coolant through the internal wall is considered, which is often referred to as the "cooling jacket" case), the terms in the above heat balance equation are given by:

$$\begin{aligned} d\dot{Q}_g &= \dot{q}_g \pi D \cdot dx_a \\ d\dot{Q}_c &= \dot{q}_c \pi D_{ext} \cdot dx_a \end{aligned} \tag{15}$$

where $\dot{q}_g$is the convective heat flux from the hot gas to the wall, $\dot{q}_c$ is the convective heat flux from the wall to the coolant, D is the internal nozzle diameter, D_{ext} is the external nozzle diameter, and dx_a is the elemental nozzle axial length. The conduction heat transfer through the nozzle wall rate can be expressed as:

$$d\dot{Q}_w = \frac{2\pi k_w}{\ln\left(D_{ext}/D\right)}\left(T_{w,g} - T_{w,c}\right) \cdot dx_a \tag{16}$$

where $T_{w,g}$and $T_{w,c}$ are the wall temperatures at the hot-gas side and at the coolant side, respectively, k_w is the wall thermal conductivity. Variable properties of graphite with temperature are considered (Ref. [22]); temperature trends of thermal diffusivity and conductivity are shown in Figure 14.

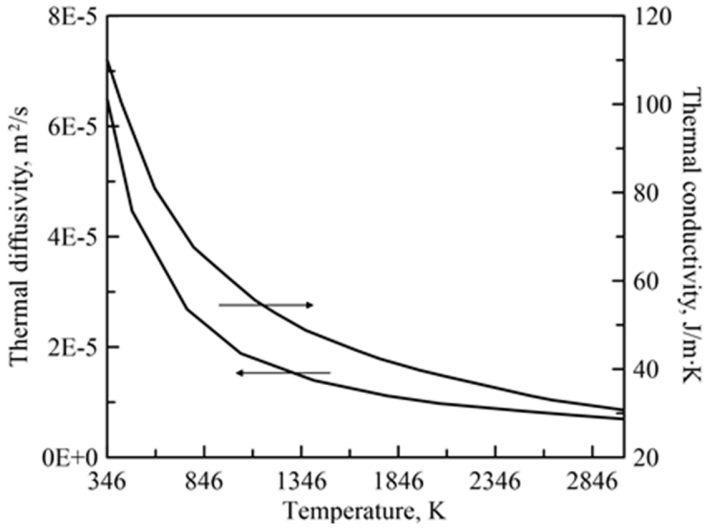

Figure 14 Graphite thermal properties with density equal to 1850 kg/m^3.

The convective heat flux to the inner nozzle wall and that to the coolant are, respectively, computed by means of the following equations:

$$\begin{aligned} \dot{q}_g &= \eta_{tot}\dot{q}_b = \eta_{tot} h_g (T_{aw} - T_{w,g}) \\ \dot{q}_c &= h_c (T_{w,c} - T_c) \end{aligned} \tag{17}$$

where T_c is the coolant bulk temperature, and T_{aw} is the adiabatic wall temperature. For the sake of simplicity, the recovery factor was assumed to be equal to 1, hence the adiabatic wall temperature is equal to the stagnation temperature, T_0, that is the flame temperature. The term, $\dot{q}_b$, is a sort of "ideal" wall heat flux determined with the well-known Bartz's equation, which is reported in the next subsection. This quantity, as will be discussed in the following, must be adjusted with the correction factor, η_{tot}.

The heat balance above is not realistic because it does not consider the enhanced heat transfer due to the presence of the fins. Using the classic fin analysis reported in Ref. [28], the fin effectiveness, ε, can be introduced, which is defined as the

ratio of the heat flux transferred through the fin to the corresponding heat flux in the absence of fin. Considering the effect of the fin, thus, the heat transfer rate from the wall to the coolant becomes:

$$d\dot{Q}_c = \dot{q}_c N_{ch} w_{ch_a} dx_a + \dot{q}_c \varepsilon N_{ch} w_{f_a} dx_a \tag{18}$$

where w_{f_a} is the fin axial width, which is equal to w_{c_a} in the present configuration. If the fin is not considered (i.e. the "cooling jacket" case is considered), $\varepsilon = 1$, and the expression above reduces to Eq. (15), being $N_{ch}\left(w_{c_a} + w_{f_a}\right) = \pi D_{ext}$. The effectiveness ε for uniform cross-section area fin with adiabatic tip is calculated as follows:

$$\varepsilon = \sqrt{\frac{2k_w}{h_c w_{f_a}}} \tanh\left(\sqrt{\frac{2h_c}{k_w w_{f_a}}} l\right) \tag{19}$$

where h_c is the coolant heat transfer coefficient, and l is the fin length (or the height of the channel). It is worth noting, here, that the elemental axial length of the channel, dx_a, is different from the corresponding length dx, for the swirl angle, (see Figure 15 in which the velocity vector components have been shown to highlight the flow direction); thus, the incident wall heat flux area is given by the product $w_{c_a} dx_a$, where dx_a is equal to $dx \sin\alpha$.

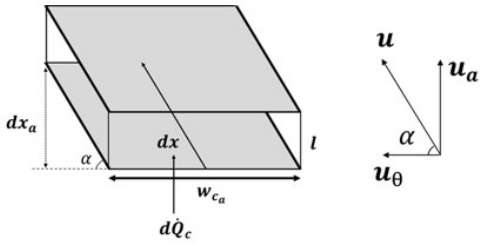

Figure 15 Schematic of the elementary spatial elements and the velocity vector components.

5.3.Coolant flow model

The coolant flow is modelled by means of the steady-state form of the mass, momentum, and energy conservation equations, taking into account the effects of heat transfer and friction. Because the coolant spins around the nozzle axis, the nature of the coolant flow field is three dimensional, but it can be simplified to one-dimensional by considering the surface area normal to the velocity vector in the relative equations. The steady-state differential continuity, momentum and energy equations governing the coolant flow through constant cross-sectional area channels are, respectively:

$$\begin{aligned} G &= const \\ \frac{dI}{dx} &= -\frac{1}{2} f \rho u^2 \frac{1}{D_h} \\ \frac{dH_0}{dx} &= \frac{\dot{Q}_c}{N_{ch}\dot{m}} = \frac{\dot{q}_c (w_{ch_a} + \varepsilon w_{f_a}) \sin\alpha}{\dot{m}} \end{aligned} \tag{20}$$

in which $G = \rho u$ is the mass flux, $H_0 = H + \frac{u^2}{2}$ is the total enthalpy defined as the sum of the sensible enthalpy and the specific kinetic energy, $I = p + \rho u^2$ is the total impulse, and $\dot{Q}_c$ is the wall heat power per unit length incident on the channel surface evaluated in the previous subsection. The terms on the right-hand-side of Eq. (20) of course represent the momentum and energy change driving factors, which are the friction losses and the convective heat flux, which imply a corresponding change in the coolant thermal properties and phase state.

Depending on the pressure-temperature history of the coolant, Eq. (20) cannot be continuously integrated along the channel, if the vapour pressure curve is crossed (see Figure 16). Indeed, as detailed below, when phase change occurs, the continuity of the fluid-dynamic properties such as pressure, temperature and density is not guaranteed.

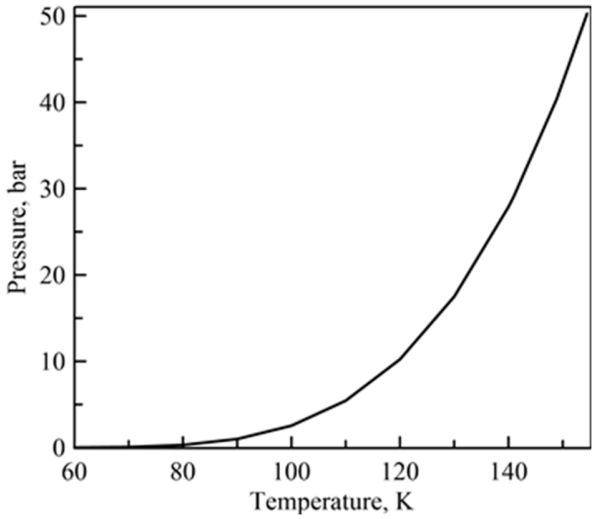

Figure 16 Oxygen phase curve.

When the vapour phase curve is crossed, all the liquid oxygen properties are stored. The evaporation mass flow rate is evaluated as follows [29, 30]:

$$\dot{m}_v = A_i G_v \tag{21}$$

where A_i is the interfacial area density and G_v is the vapour mass flux per unit length of the channel. In this study, the interfacial area density is modelled following the model proposed by Liao and Lucas [31]:

$$A_i = (6\alpha_v)^{2/3}(\pi N_b)^{1/3} \tag{22}$$

in which N_b is the number of bubbles per unit volume (bubble number density). In this work, the distribution of bubble and phenomena of bubble dynamics such as bubble break-up and coalescence are neglected. For this reason, N_b is assumed constant for all tested cases, equal to $4 \cdot 10^8 m^{-3}$. Assuming the Hertz Knudsen formula, which gives the evaporation flux based on the kinetic theory for a flat interface, the mass flux is evaluated as:

$$G_v = \beta \sqrt{\frac{M_w}{2\pi R T_{sat}}}(p_{sat} - p^*) \tag{23}$$

where $p^*$is the vapour pressure at the interface that it is assumed to be close to p_{sat}, and β is an "accommodation" coefficient, which is here assumed equal to 1. R is the universal gas constant and M_w is the molecular weight. Thus, G_v only slightly depends on the saturation temperature. All the model constants have been taken from Ref. [29], in which a series of sensitivity analyses were performed to evaluate their impact on the results. The volume fraction α_v is given by:

$$\alpha_v = \frac{X_v \rho_l}{(1 - X_v)\rho_v + X_v \rho_l} \tag{24}$$

where X_v is the vapour mass fraction (i.e. the ratio of the vapour mass flow rate to the total one), ρ_v and ρ_l are the gas and liquid density, respectively. Then, the mixture properties, such as viscosity, are evaluated as weighted average of the gaseous volume mass flow rate. Finally, the heat loss due to mass flow rate vaporization is added as source term on the right-hand-

side of the energy equation in (20). For additional details, the reader can find the basic multiphase relations of the homogeneous mixture model in Ref. [32].

5.4. Friction and heat transfer correlations

Because of the simplifications introduced by the one-dimensional model, semi-empirical correlations are required for the modelling of the hot-gas heat transfer coefficient, h_g, friction coefficient, f, and the coolant heat transfer coefficient, h_c. The latter two coefficients are evaluated through the following equations [33]:

$$\begin{aligned} f &= f^0 \left(\frac{T_{w,c}}{T}\right)^{-0.52} \\ Nu &= Nu^0 \left(\frac{T_{w,c}}{T}\right)^{-0.47} \end{aligned} \tag{25}$$

where f^0 and Nu^0 are, respectively, the local reference skin friction coefficient and Nusselt number evaluated at constant fluid properties (i.e. with no temperature gradient along the radial coordinate), whereas the temperature ratios are corrective terms accounting for the temperature non uniformity across the channel section, *T* has to be intended as the bulk temperature in the section. f^0 is evaluated by means of a modified version of the Colebrook's semiempirical relation for multiphase flows [34] with a roughness height, ε_w, of 10 μm, which was estimated by means of previous cold flow tests performed with water in the absence of combustion:

$$\frac{1}{\sqrt{f^0}} = 3.48 - 4\log_{10}\left(\frac{2\varepsilon_w}{D_h} + \frac{9.35}{Re\sqrt{f^0}}\right) \tag{26}$$

Nu^0 is evaluated as follows [35] :

$$Nu^0 = \frac{(f^0/2)RePr}{1 + \sqrt{f^0/2}(4.5Re_\varepsilon^{0.2}Pr^{0.5} - 8.48)} \tag{27}$$

where Re_ε is the roughness Reynolds number defined as $Re_\varepsilon = Re(\varepsilon_w/D)\sqrt{f^0/2}$. Once the Nusselt number is calculated, the coolant heat transfer coefficient can be immediately computed: $h_c = Nu \cdot k_c/D_h$. Regarding the hot gas heat transfer coefficient, the Bartz equation was used in this work, which is given by:

$$\begin{aligned} h_g &= \left[\frac{0.026}{D_t^{0.2}}\left(\frac{\mu^{0.2}c_p}{Pr^{0.6}}\right)_0 \left(\frac{p_c}{c^*}\right)^{0.8}\left(\frac{D_t}{R_c}\right)^{0.1}\right]\left(\frac{A_t}{A}\right)^{0.9}\sigma \\ \sigma &= \left\{\left[\frac{1}{2}\frac{T_{w,g}}{T_0}\left(1 + \frac{\gamma-1}{2}M^2\right) + \frac{1}{2}\right]^{0.68}\left[1 + \frac{\gamma-1}{2}M^2\right]^{0.12}\right\}^{-1} \end{aligned} \tag{28}$$

where c^* is the characteristic exhaust velocity, R_c is the nozzle throat radius of curvature, A_t is the nozzle throat area, and A is the nozzle local cross-sectional area. The term $(D_t/R_c)^{0.1}$ is on the order of 1 and has been neglected. Because the viscosity, the specific heat and the Prandtl number do not change dramatically with the static temperature along the rocket nozzle, the ratio $\mu^{0.2}c_p/Pr^{0.6}$ is maintained constant and evaluated at the stagnation temperature. The local hot-gas parameters appearing in Eq. (28) are estimated via the one-dimensional isentropic flow equations; the wall heat flux can, then, be calculated at each axial position as a function of the unknown temperature, $T_{w,g}$.

Bartz's formula can introduce huge uncertainties, and for this reason, it needs to be corrected. Following Eq. (17), the convective wall heat flux can be written as:

$$\dot{q}_g = \eta_h h_g\left(\eta_T T_0 - T_{w,g}\right) \tag{29}$$

where$\eta_T$and η_h are defined as follows:

$$\eta_T = \frac{T_{0,exp}}{T_0} \cong \left(\frac{c^*_{exp}}{c^*_{id}}\right)^2, \qquad \eta_h = \frac{h_{g,exp}}{h_{g,B}} \tag{30}$$

The temperature efficiency, η_T, is related to the deviation of the experimental temperature from the equilibrium combustion temperature calculated at the measured average mixture ratio and chamber pressure; η_h takes into account the deviation between the experimental heat transfer coefficient and that computed with the Bartz's formula. Note that, as the hot-gas wall temperature is significantly lower than the stagnation temperature, one can approximately introduce an overall efficiency, $\eta_{tot} = \eta_h \eta_T$, which represents the ratio of the actual heat flux to the one calculated with the Bartz'z formula in ideal combustion conditions.

The value of η_T was estimated by matching the experimental data acquired in Tests NC; Test AC1 and Test AC2 then allowed using for the following calculations a more reliable approximation of the hot gas convective coefficient computed with Eq. (28).

5.5.Numerical methods and procedures

In this section, the numerical technique used for the calculations of the steady-state heat transfer and the integration of the coolant equations is described. A flowchart is provided in Figure 17 to show the main steps of the overall solution procedure. The coolant properties have been tabulated for a number of coolant pressures and temperatures in order to save computational time. The final property table is an ensemble of the following three sub-tables: the liquid-like, the gaseous-like, and the supercritical tables. A flag is set to indicate the fluid phase and to select the proper property table. Once the geometrical parameters given in subsection 3.1 are specified, and the initial coolant condition is defined, the main computational algorithm is run. At the beginning of the n^{th}-step, the total coolant enthalpy and impulse are known. The following system of four algebraic non-linear equations has to be solved for pressure, density, temperature and enthalpy:

$$\begin{aligned} p + \frac{G^2}{\rho} - I &= 0 \\ H + \frac{G^2}{2\rho^2} - H_0 &= 0 \\ \rho &= f(p,T) \\ H &= f(p,T) \end{aligned} \tag{31}$$

The solution provides, thus, the coolant pressure and temperature condition corresponding to the given state of total impulse, total enthalpy and mass flux; the coolant temperature, in particular, is required to solve the heat transfer problem. The heat transfer problem is solved using Eq. (15) and Eq. (18), which give the internal nozzle temperature, the external temperature, and the wall heat power transferred from the hot to the coolant side, which is required for the integration of the coolant equations (Eq. (20)). Then, the total impulse and enthalpy are updated. At this point, pressure and temperature are checked. If the vapour curve is crossed, the vaporization model is called by Eq. (21), and the gaseous state flag is imposed. For the sake of simplicity, the coolant differential equations have been integrated with a first-order Euler scheme. However, a dedicated error study was performed to select a suitable spatial step ensuring a good accuracy. Once obtained the new I and H_0, the solution procedure is repeated until the exit section of the channel is reached.

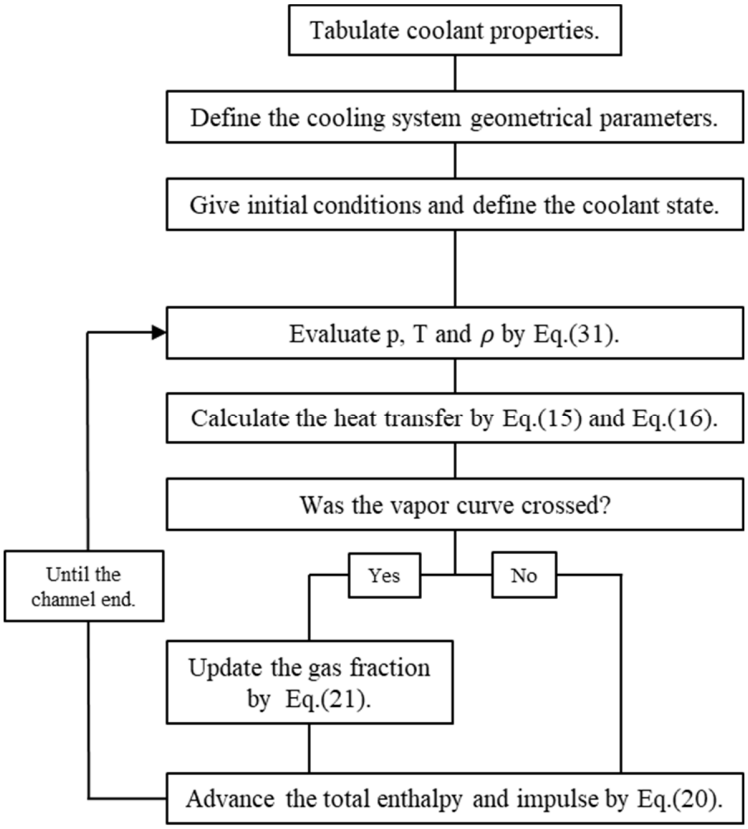

Figure 17 Flowchart of the numerical procedure.

6. Numerical Results

In this section, the numerical results are presented following the three logical steps listed below.

- First, the incoming convective heat flux from the combustion gases is corrected by tuning the constant η_{tot} based on the experimental data retrieved from Test NC (which is carried out with no nozzle cooling system).
- Second, the overall numerical model is assessed against the experimental data.
- Third, a series of parametric analyses are performed to explore the coolant efficiency in the supercritical state and make a comparison with the subcritical case to investigate into the effect of the number of channels, which is the main geometrical parameter.

6.1. Wall heat flux estimation

An estimation of the heat flux transferred from the hot gas to the graphite nozzle is here carried out, by means of matching the calculated temperature field in the nozzle wall with the three temperature profiles measured at the throat section. Test NC is used as a test case for the evaluation of η_h in Eq. (29). A 2D axisymmetric transient numerical simulation is needed to obtain the time evolution of the temperature field in the nozzle, because the nozzle has a short length-to-diameter ratio as well as a prominent two-dimensional geometry. The following energy balance equation in the solid domain is solved:

$$\frac{\partial \rho e}{\partial t} = \frac{\partial}{\partial z}\left(k_w \frac{\partial T}{\partial z}\right) + \frac{1}{r}\frac{\partial}{\partial r}\left(k_w r \frac{\partial T}{\partial r}\right) \tag{32}$$

where e is the internal energy, z is the axial coordinate, and r is the radial coordinate. A convective heat transfer boundary condition was set to the inner wall exposed to the hot gas. Adiabatic boundary conditions were set at all the other walls. The initial condition was set to the room temperature. The convective heat transfer coefficient h_g was iteratively adjusted because of its dependence on the temperature of the nozzle wall exposed to the hot gases. A parametric analysis was performed to find the most suitable value of η_h that ensures matching the measured temperatures in the nozzle with those computed by the heat-transfer transient simulation: η_h was calculated to be 0.17, which means that the convective heat transfer coefficient estimated with the Bartz's formula is around six times higher than that occurring in the firing test. However, note that this parameter has to be interpreted as a fitting coefficient to reproduce the experimental data, and its value does not actually provide the exact magnitude of the deviation of the heat transfer evaluated with the Bartz equation and the one occurring in the nozzle, because of the assumptions behind Eq. (29); for instance, the adiabatic wall temperature has been approximated with the stagnation temperature, which implies underestimating η_h. η_{tot} is thus equal to 0.12. The time-averaged incident wall heat flux is estimated to be around 1.6 MW/m^2.

In Figure 18 the time trend of the temperature measured in the nozzle at 3 mm far from the throat surface is compared with that calculated. A good match between the numerical and the experimental profile is shown. In particular, a temperature of 1000 K is reached by both curves at the end of the burning time. Figure 19 depicts the hot-gas heat transfer coefficient, h_g, along the nozzle axis. According to Eq. (28), a peak of 1200 W/m^{2}K in the nozzle throat section, where the gas mass flux is maximum. Figure 20 represents the temperature contour obtained after 20 s. The temperature field is far from being uniform for the two-dimensional nozzle shape. The temperatures achieved in each nozzle section mainly depend on the local convective heat transfer coefficient and on the nozzle thickness. Although the throat section is subjected to the highest convective heat transfer, the temperature calculated at the cooling side wall is lower than that at the convergent section, which is due to the lower nozzle wall thickness. Accordingly, the nozzle divergent portion is the coolest zone with temperatures below 900 K.

The computed η_h will be enforced in the next analysis to correct the overall heat flux and to assess the numerical model results against the experimental data.

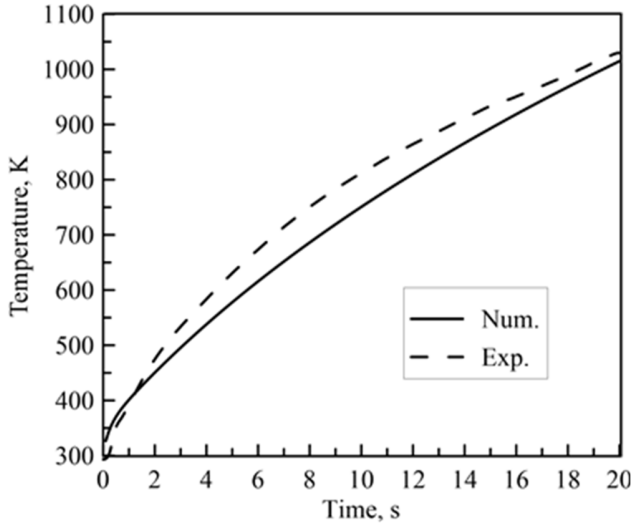

Figure 18 Comparison between the experimental and numerical temperature profiles at 3 mm from the nozzle throat.

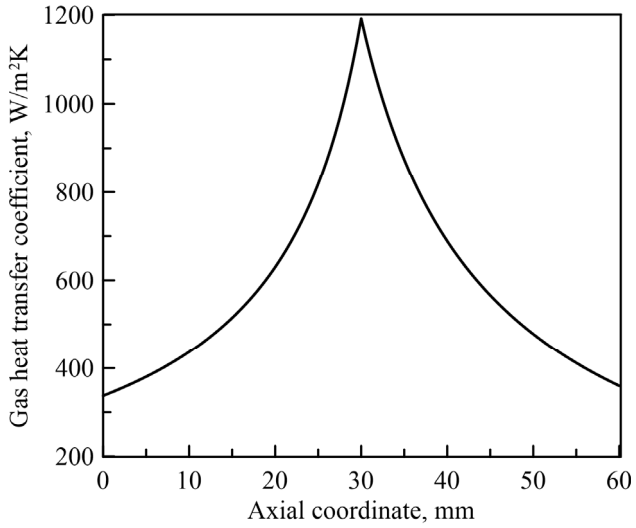

Figure 19 A representation of the heat transfer coefficient corrected by the total efficiency, η_{tot}.

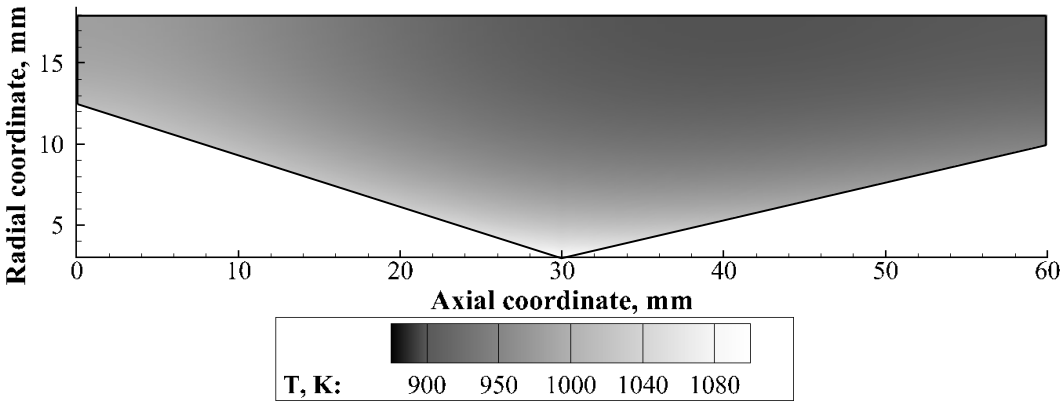

Figure 20 Nozzle temperature-contour plot at the end of the transient simulation (burning time 20 s).

6.2.Cooling model assessment

Here the numerical model capability is assessed by comparing the numerical results with the experimental data. Figure 21 represents the comparison of the measured and calculated temperatures obtained along the nozzle thickness in correspondence with the throat. The hot side of the graphite nozzle reaches a temperature peak of 700 K at the throat section, with a temperature decrease across the nozzle thickness of around 170 K. The main deviation is observed near the throat (at 3 mm distance), where the nozzle shape is far from the one-dimensional idealization. The local shape produces an axial component of the incident heat flux leading to an overheating, especially in the region near the throat, which cannot be taken into account by the 1D heat transfer model. The coolant properties and fluid dynamic quantities have been integrated with a spatial step of 5 mm; the resulting accuracy is discussed in the next subsection. It is worth pointing out that, because the coolant flows towards the entrance of the nozzle, the coolant channel axial coordinate is reversed with respect to the nozzle axial coordinate. In addition, all the results of the cooling code are shown along the axial projection of the curvilinear helical channel. Figure 22 depicts the pressure and temperature profiles over the channel axis along with the gaseous volume fraction. As shown, the gaseous flow rate steeply increases at the throat (which is located at 30 mm), where the largest heat transfer is reaches the coolant. An outlet volume fraction of 0.97 is computed in the current test case. The liquid vaporization begins at 15 mm from

the inlet (the oxygen vapour phase curve is crossed at this point). Downstream of the throat, the coolant is mostly in the gaseous phase: the pressure rapidly decreases (i.e. pressure drop increases) because of the reduction of the fluid density; in the same way, the coolant temperature rapidly increases because of the lower fluid specific heat (which, in the gaseous phase, is half of the liquid one). The deviation of the calculated exit temperature from the experimental value is around 7%, whereas the one of pressure is about 4%. An underestimation of these quantities was expected because the channels are not completely isolated from the environment. Figure 23 displays a comparison of the nozzle wall temperatures at the hot and cold sides with the computed liquid heat transfer coefficient. In particular, h_c increases in the first portion of the channel, upstream of the onset of vaporization, for the growth of the Reynolds number. The profile is mostly affected by the wall temperature due to the dependency shown in Eq. (25). The nozzle throat section is, as expected, the most critical one because it is subjected by the highest convective heat flux from the hot gas and the worst cooling performance from the coolant side with a drop of h_c from about 4000 to around 2900 W/m^{2}K

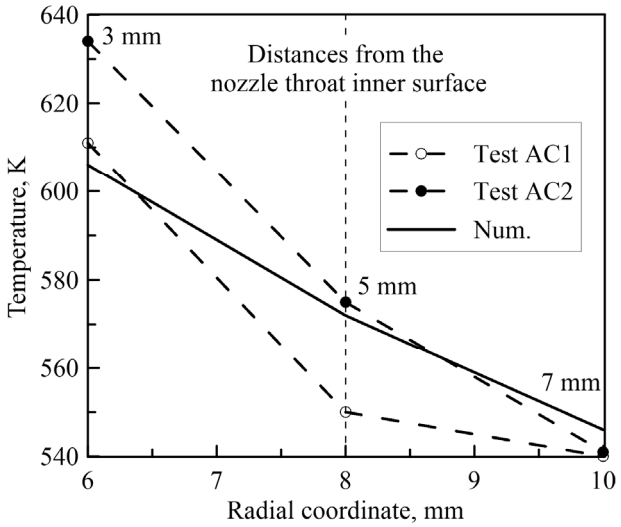

Figure 21 Comparison between the experimental and numerical temperatures at 3, 5 and 7 mm from the nozzle throat in Test AC1 and AC2.

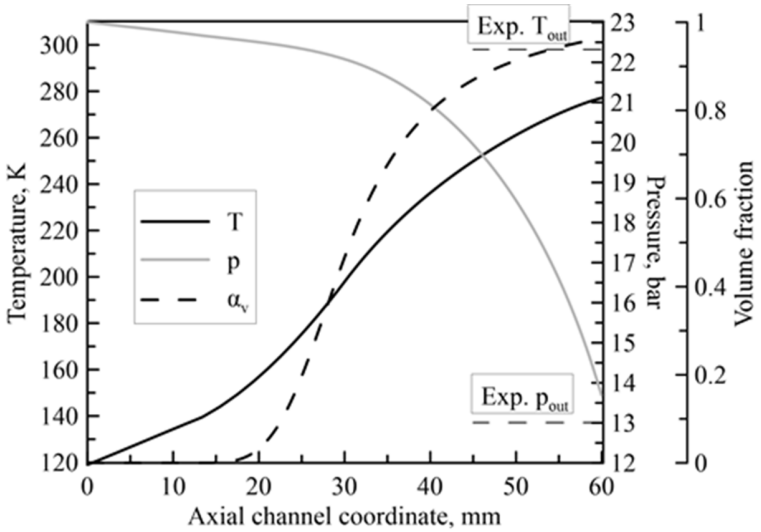

Figure 22 Pressure and temperature profiles along the cooling channel and comparison with the experimental data of Test AC2.

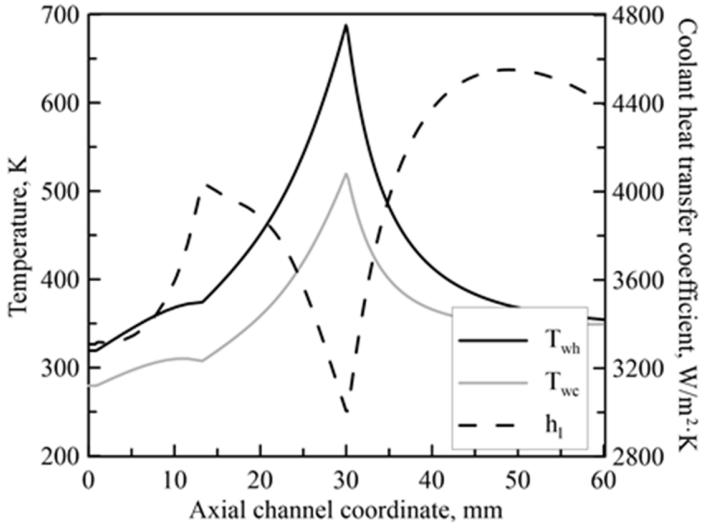

Figure 23 Nozzle wall temperatures and liquid heat transfer coefficient profiles.

6.3. Steady state analysis

6.3.1. Numerical error analysis

The dependence of the solution on the spatial discretization is analysed in this subsection. The temperature profiles calculated with three different spatial steps are here compared; step sizes are set to 2.5 mm, 5 mm, and 10 mm. The number of channels was imposed equal to three in the analysis, and the coolant initial pressure and temperature were imposed equal to 23 bar and 119 K, respectively. The nozzle geometry shown in the previous section is maintained. Figure 24 shows the

three profiles obtained using the three different numerical grids. As shown, the solutions are practically overlapped, demonstrating that the accuracy of the considered spatial discretization step size of 5 mm is satisfactory.

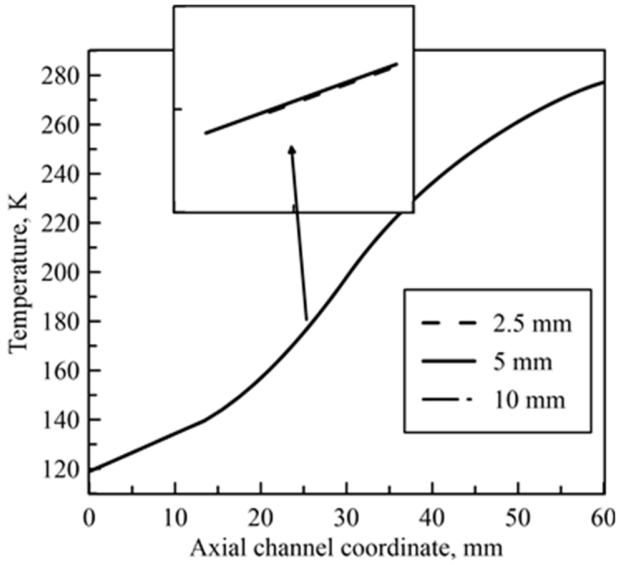

Figure 24 Coolant temperature profiles calculated with three different spatial steps.

6.3.2. Supercritical case

In this section, steady-state analyses are shown in order to understand the key concepts to improve the current cooling system. The first analysis was performed by setting a mass flow rate and a wall heat flux efficiency equal to the previous test case discussed in Subsection 6.2. The inlet pressure, temperature and mass flow rate were set to 55 bar, 119 K and 12 g/s, respectively. Figure 25 depicts the evolution of the main thermo-fluid-dynamic parameters along the channel. The fluid density largely changes along the axial channel coordinate from 1020 to 100 kg/m^3. No discontinuity is shown by the fluid dynamic quantities because the vapour curve is not crossed (see Figure 26). When the fluid state is near to the critical point, (at which pressure is equal to 50 bar and temperature equal to 154 K), the coolant behaviour changes from liquid-like to gaseous-like. The “phase change” occurs at the throat section, where the coolant is heated the most. Indeed, downstream of this point, the velocity and the temperature strongly increase from 4 to 27 m/s, the temperature grows by 60 K and the pressure drops by around 5 bar (around half of the previous test case).

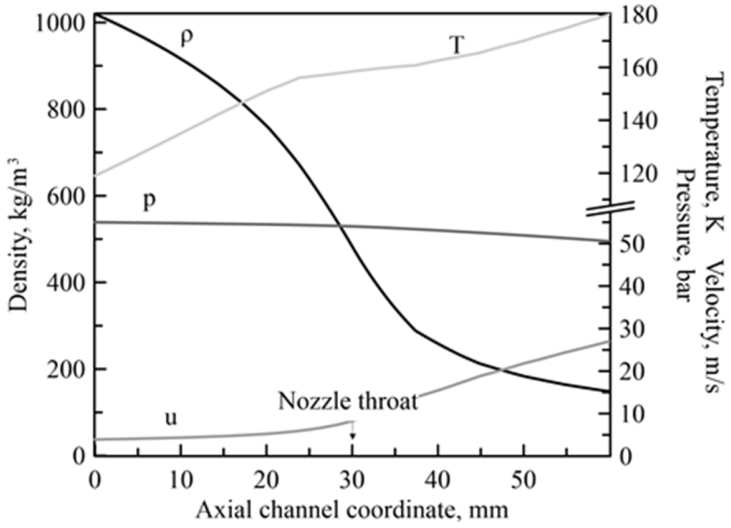

Figure 25 Coolant density, pressure, temperature, and velocity evolution along the channel.

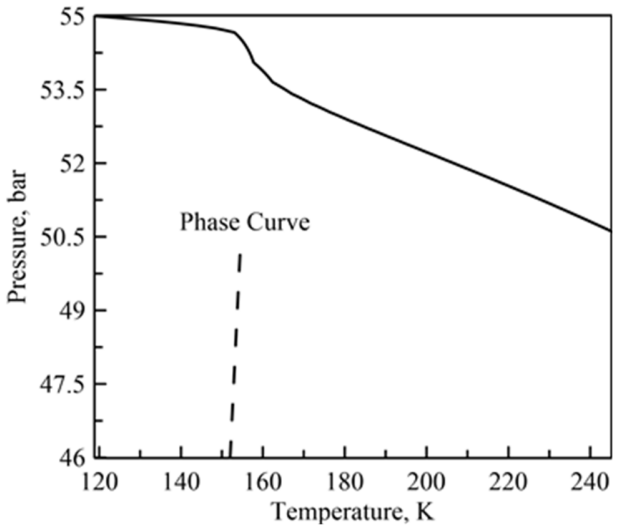

Figure 26 Coolant pressure vs temperature curve and oxygen vapour curve.

Regarding the heat transfer analysis, Figure 27 represents the nozzle temperatures at both the hot and cold sides. Temperatures of 250 K and 400 K are reached at the nozzle throat at the cold and hot sides, respectively. In addition, the largest temperature difference across the nozzle wall is observed right in this section, where the nozzle wall has the maximum thickness. The most critical temperatures are achieved in the divergent portion, rather than in the throat, with 425 K on the hot side. The nozzle wall temperature depends on both the convective heat transfer coefficients on the hot and cold sides. The throat is still the most heated zone but, in this test case, it is also largely cooled down; Figure 27b displays a coolant heat transfer coefficient of $1.25 \cdot 10^4$ W/m^{2}K at the nozzle throat, which is close to the maximum value along the cooling channel. This is in line with the objective of the cooling system, which is designed to drastically cool down the nozzle throat wall and suppress thermochemical erosion.

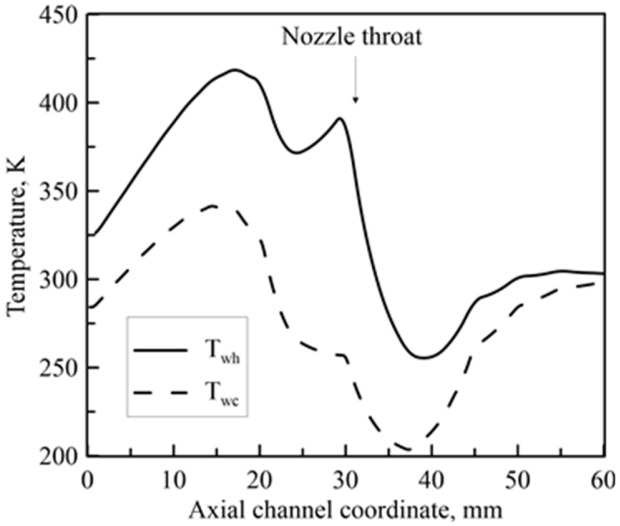

(a) Nozzle wall temperatures at both the hot and the cold sides.

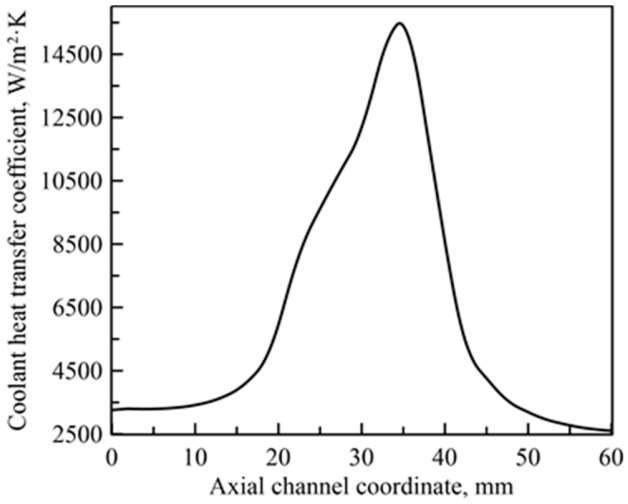

(b) Coolant heat transfer coefficient.

Figure 27. Nozzle temperatures and coolant heat transfer coefficient along the nozzle channel ($\mathbf{p_{in} = 55\ bar, T_{in} = 119\ K,\ \dot{m} = 12\ g/s}$).

Finally, Figure 28 represents the sensible enthalpy and a comparison of the coolant specific heat in subcritical and supercritical conditions. The specific heat is, of course, one of the most critical parameters for the cooling system design, as larger specific heat implies larger capacity of the cooling system to absorb heat. In the current test case, the specific heat ranges between 1900 and 8000 J/kg·K with the peak in correspondence of the nozzle throat. The pseudo-boiling occurs right in this zone where the "phase change" occurs when the static enthalpy is zero. Crossing the critical point improves the performance of the cooling system. Indeed, the computed exit temperature is around 100 K lower than that computed in the previous section. This improvement is not observed in the subcritical case.

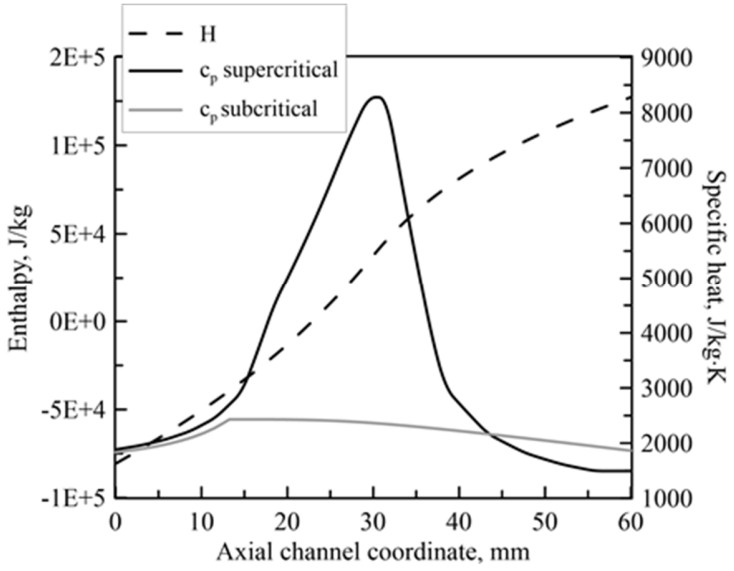

Figure 28 Coolant enthalpy and specific heat in the cooling channel.

6.3.3. Effect of the inlet pressure and temperature

Results from the test case previously shown for the model assessment are here compared with an additional hypothetical test case with the higher inlet pressure of 28 bar, assuming the same pressure drop of 9.5 bar. The convective heat transfer from the combustion gases is estimated by scaling the chamber pressure in Eq. (28) for the calculation of h_g with the computed mass flow rate of 21 g/s. Figure 29a represents the density and gas volume fraction in the two tests. The vaporization starts a few millimetres downstream of the point relative to the case performed with an inlet pressure of 23 bar because the saturation curve is crossed at a higher temperature by increasing the inlet pressure. Therefore, the timing for the vaporization decreases, and the exit α_v drops from 0.96 to 0.80. As a consequence, the average density is higher in the test case with p_{in} at 28 bar resulting in a higher mass flow rate with a consequent increase of the engine thrust. In addition, Figure 29b displays the temperatures achieved on the nozzle wall from the hot side, which are mostly overlapped despite the mass flow rate through the engine nozzle in the test performed with p_{in} = 28 bar is 70% higher than that with $p_{in} = 23$ bar. The larger heat flux to the nozzle wall occurring for the larger mass flow rate is absorbed by the cooling system, whose performance, thus, scales with the engine thrust. For this reason, it can be said that the system is "throttleable" from a thermal point of view because an increase of thrust does not lead to a nozzle overheating.

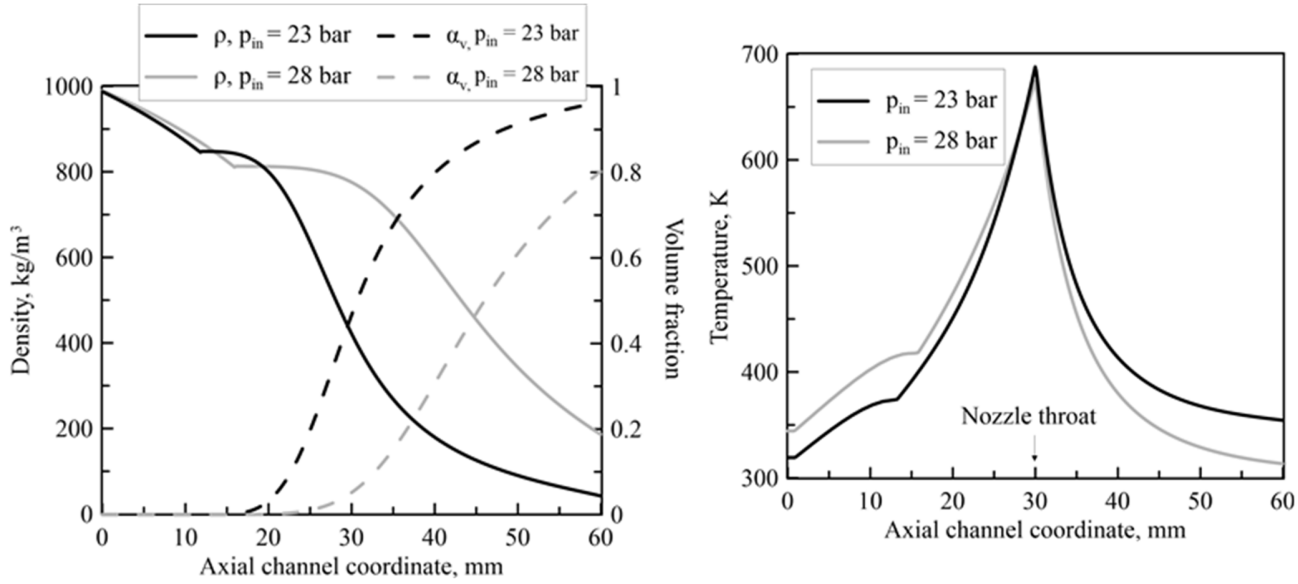

(a) Coolant density and volume fraction. **(b) Hot side nozzle wall temperature.**

Figure 29 A comparison of the numerical results obtained by enforcing an inlet pressure of 23 and 28 bar ($T_{in} = 119\ K$).

Now, the effect of the inlet temperature is investigated. Assuming an inlet pressure of 23 bar and a temperature of 105 K, a mass flow rate of 21 g/s is obtained again. The results are compared with those obtained with the inlet pressure and temperature of 28 bar and 119 K. Figure 30a depicts the computed volume fraction and the coolant heat transfer coefficient in the two test cases. As shown, the vaporization starts approximately at the same axial channel coordinate leading to the same exit gas volume fraction near 0.8. However, the liquid heat transfer coefficient in the case of the lower inlet temperature is degraded of 25 %. Indeed, observing Eq. (25), a larger difference between the coolant temperature and the wall temperature involves higher reduction of h_c. Consequently, the nozzle temperature obtained at the throat is 100 K higher in this configuration with a peak of 750 K. Although it is unreasonable to increase the mass flow rate by decreasing the temperature, the current calculation demonstrates that the mass flow rate in subcritical conditions is extremely sensitive to the inlet temperature, pointing out the difficulties encountered in performing experimental tests. Therefore, hybrid rocket engines using

regenerative cooling require advanced isolation systems in order to control the oxidizer mass flow rate by the pressurization system and achieve the expected propulsion performance.

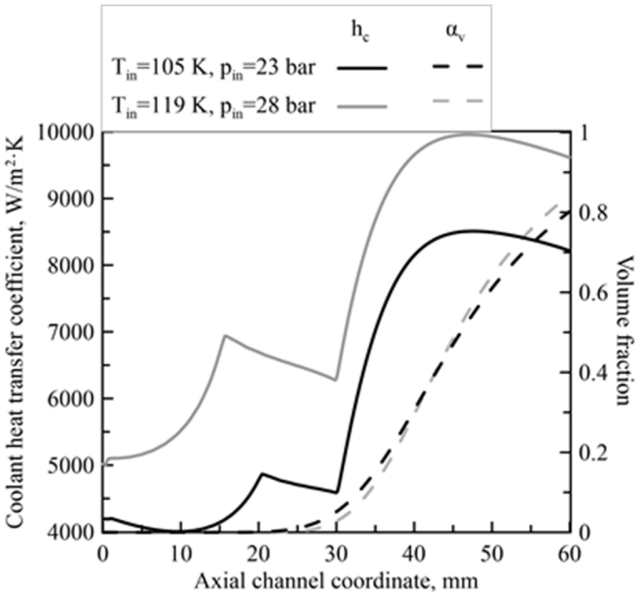

(a) Coolant heat transfer coefficient and volume fraction.

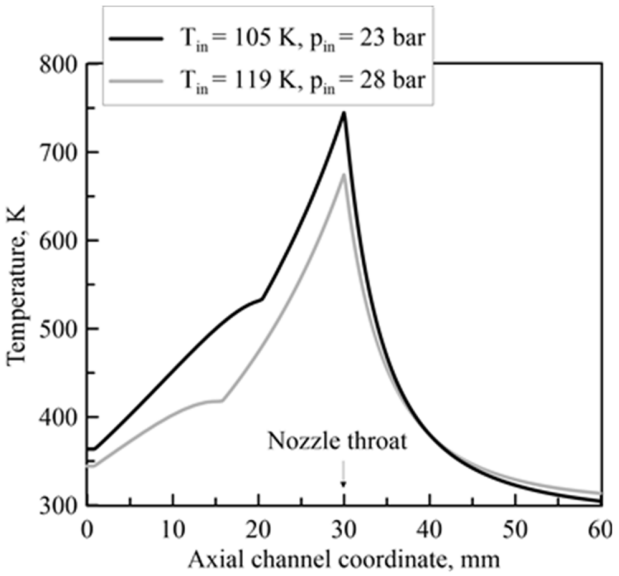

(b) Nozzle wall temperature at the hot side.

Figure 30 A comparison of the numerical results obtained by enforcing an inlet pressure of 105 and 119 K ($p_{in} = 28\ bar$).

6.3.4. Effect of the number of channels

In this section, the inlet pressure and temperature were kept equal to 23 bar and 119 K. The number of cooling channels was first doubled from 3 to 6, then was set to the maximum allowable value of 8 channels, after which the chamber pressure overcomes the inlet pressure. The corresponding channel lengths are 1130, 565 and 424 mm, and the mass flow rate per channel of 4 g/s was maintained constant in all the test cases. Figure 31 represents a comparison of the hot side nozzle temperature, liquid heat transfer coefficient and pressure drop among the three cases. It can be noticed that increasing the number of channels from 3 to 6 results in an increase in nozzle temperature at the hot side of around 500 K. In contrast, an additional temperature augmentation of around 200 K is obtained by increasing the number of channels from 6 to 8. This is a counter-intuitive result, indeed a higher number of channels in the case of axial channels leads to an enhancement of the cooling performance because of the reduction of the channel area. In the case of the helical channels, a higher number of cooling channels entails a reduction of the swirl angle and of the wet surface per channel (see Figure 8), while the channel cross-sectional area remains unaltered. The reduction of the wet surface with increasing the number of channels leads to the decreasing trend of the heat absorbed per unit of flow rate, as shown in Figure 31b. Figure 31c displays the coolant heat transfer coefficient axial profiles computed in the three configurations by highlighting the effect of the temperature non-uniformity in the channel section introduced through Eq. (25). If the latter effect is not taken into account, the average coolant heat transfer coefficient increases with the number of channels. In fact, the largest gas fraction and, consequently, the lowest Prandtl number are calculated with three channels, which thus lead to the lowest value of h_c. However, the configuration

leading to the largest gas fraction also features the highest coolant temperature. As a result of Eq. (25), these two competing effects are such that the average h_c along the channel length is higher in the configuration with the fewest channels.

Regarding the pressure and the gas volume fraction, the former drops from 13.5 to 1 bar when increasing from 3 to 6 channels and 0.5 bar in the case of 8 channels, whereas the latter progressively decreases from 0.96 to 0.70 to 0.4.

In summary, a benefit in terms of pressure drop is observed by adding channels to the cooling system; however, critical thermal drawbacks are shown, increasing the probability of nozzle erosion to occur. Indeed, assuming the erosion onset temperature equal to 1400 K as reported in Ref. [8], eight represents the maximum allowed number of channels in order to suppress nozzle erosion. In this scenario, the minimum number of channels that matches the chamber pressure requirement is the best option. This minimum value is expected to increase with the engine thrust class because larger thrust levels require larger mass flow rates and nozzle dimensions which, then, imply higher coolant pressure drops.

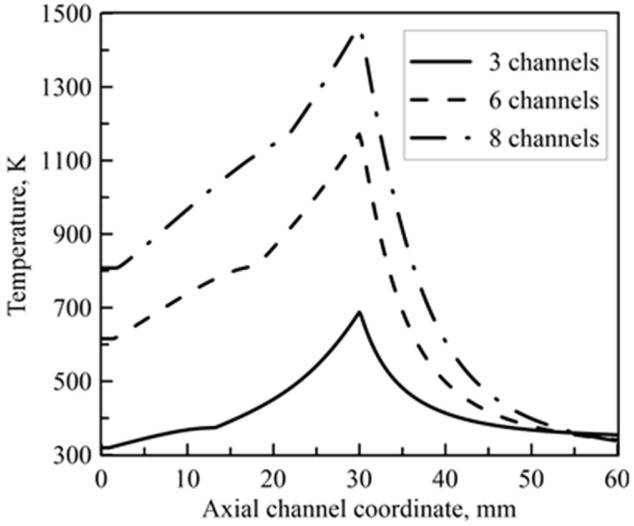

(a) Hot side nozzle wall temperature.

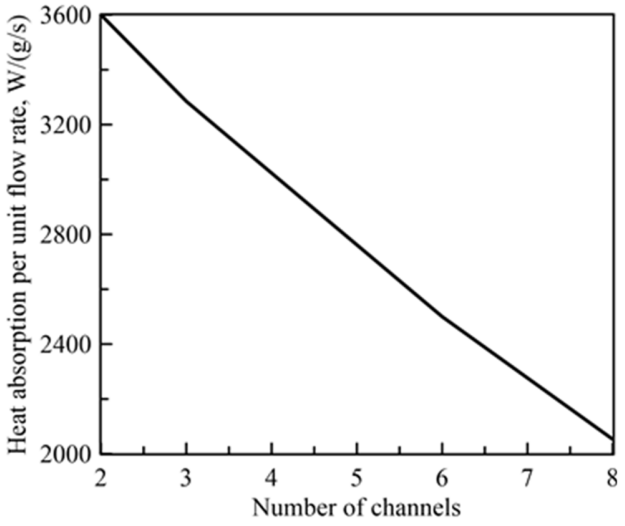

(b) Heat absorption per unit of flow rate.

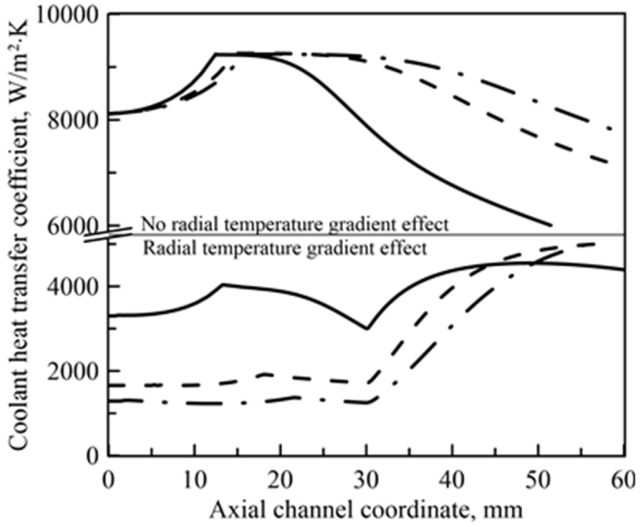

(c) Liquid heat transfer coefficient.

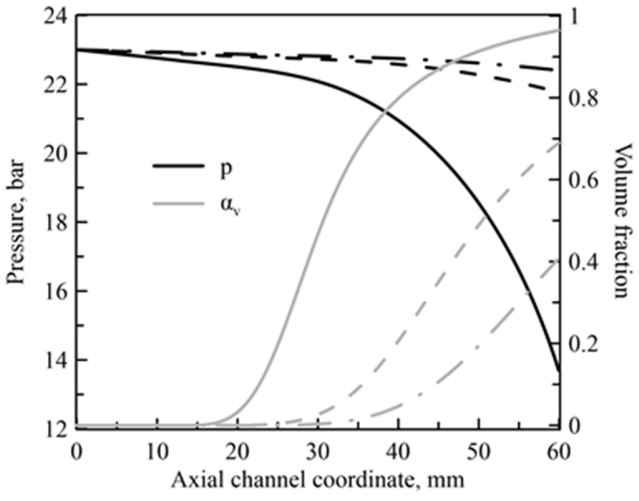

(d) Pressure drop and volume fraction.

Figure 31 Effect of the number of channels.

7.Conclusions

In the present work a one-dimensional numerical model for the study of the performance of a cooling system based on helical channels wrapping on the exhaust nozzle of a hybrid rocket is addressed. Liquid oxygen is used for the coolant. The numerical model prediction capability was assessed with the experimental results of two firing tests carried out with equal operating conditions: one without nozzle cooling, and the other with nozzle cooling First, a comparison with the nozzle wall temperatures measured in the test in the absence of cooling allowed calibrating the incoming wall heat flux from combustion gases estimated with the Bartz formula, which was estimated to be around 1.6 MW/m^2 in the nozzle throat section. Second, three analyses were carried out by varying the coolant conditions and the number of cooling channels. The first analysis showed the heat transfer enhancement obtained by feeding the coolant in supercritical conditions. The second highlighted the effect of increasing the inlet pressure and decreasing the inlet temperature when the coolant is injected in subcritical conditions. Finally, the last analysis showed the improvements and the drawbacks obtained by increasing the number of channels from 3 to 6 and, then, to 8, which is the maximum allowable number of channels in the present configuration. The pressure drop decreases with the number of channels from 13.5 to 1 bar and then to 0.5 bar; the exit gas volume fraction decreases from 0.96 to around 0.7 and then to 0.4. The nozzle temperature increases by 500 K by increasing the number of channels from 3 to 6, and by 200 K from 6 to 8, while a decreasing heat absorption per unit flow rate was shown, which dropped from 3600 to 2000 W/(g/s).

8. Acknowledgement

This research was supported by the Ministry of Education, Science, Sports and Culture Grants-in-Aid for Young Scientists 20K14946, 2020 and Japan Society for the Promotion of Science (JSPS). The authors would like to thank the master student Hiroki Kojima the support in performing the experimental campaign, whose results have been used for the validation of the presented work.

Appendix A. Real gas EOS and transport properties of oxygen

The Modified Benedict-Webb-Rubin equation of state is a multiparameter EOS, explicit in pressure. It can be written as:

$$p = \sum_{n=1}^{9} \rho^n F_{n-1} + e^{-\delta^2} \sum_{n=10}^{15} \rho^{2n-17} F_{n-1} \tag{1.A}$$

Where $\delta = \rho/\rho_c$ and ρ_c is the critical density. The functions F_n depend on the temperature, density, and a set of coefficients fit for a particular species. The expressions for the derivatives and integrals required to determine real gas thermodynamic state variables are given here [26].The functions, their temperature derivatives and the involved constants are given in Table 3 and Table 4. In order to calculate values for specific enthalpy, specific internal energy, specific heats, specific entropy, and speed of sound, Eqs. (7)-(11), certain derivatives and integrals with respect to the EOS need to be evaluated. The partial differential $(\partial p/\partial T)_\rho$ is required to calculate specific isobaric heat capacity and the specific enthalpy:

$$\left(\frac{\partial p}{\partial T}\right)_\rho = \sum_{n=1}^{9} \rho^n \frac{\partial F_{n-1}}{\partial T} + e^{-\delta^2} \sum_{n=10}^{15} \rho^{2n-17} \frac{\partial F_{n-1}}{\partial T} \tag{2.A}$$

In addition, the specific isochoric heat capacity requires:

$$\left(\frac{\partial^2 p}{\partial T^2}\right)_\rho = \sum_{n=1}^{9} \rho^n \frac{\partial^2 F_{n-1}}{\partial T^2} + e^{-\delta^2} \sum_{n=10}^{15} \rho^{2n-17} \frac{\partial^2 F_{n-1}}{\partial T^2} \tag{3.A}$$

In the real gas equations of the speed of sound and the specific isobaric heat capacity the partial differential $(\partial p/\partial \rho)_T$ is required and it is given by:

$$\left(\frac{\partial p}{\partial \rho}\right)_T = \sum_{n=1}^{9} n\rho^{n-1} F_{n-1} + e^{-\delta^2} \sum_{n=10}^{15} \rho^{2n-18} F_{n-1} \left[-\frac{2\rho}{\rho_c^2} + (2n-17)\right] \tag{4.A}$$

Similarly, certain integrals need to be solved. The integral appearing in Eq.(7) for the specific enthalpy is calculated as:

$$I_1 = \int_0^\rho \left[\frac{p}{\rho^2} - \frac{T}{\rho^2}\left(\frac{\partial p}{\partial T}\right)_\rho\right] d\rho \tag{5.A}$$

This can be rewritten in terms of the functions F_n of the MBWR EOS:

$$I_1 = \int_0^\rho \left[\sum_{n=1}^{9} \rho^{n-2} F_{n-1} + e^{-\delta^2} \sum_{n=10}^{15} \rho^{2n-19} F_{n-1} - T \sum_{n=1}^{9} \rho^{n-2} \frac{\partial F_{n-1}}{\partial T} - T e^{-\delta^2} \sum_{n=10}^{15} \rho^{2n-19} \frac{\partial F_{n-1}}{\partial T}\right] d\rho \tag{6.A}$$

The terms with $n = 1$ are equal to:

$$\frac{F_0}{\rho} - \frac{T}{\rho}\frac{\partial F_0}{\partial T} = 0 \tag{7.A}$$

Then

$$I_1 = \int_0^\rho \left[\sum_{n=2}^{9} \rho^{n-2} \left(F_{n-1} - T\frac{\partial F_{n-1}}{\partial T}\right) + e^{-\delta^2} \sum_{n=10}^{15} \rho^{2n-19} \left(F_{n-1} - T - T\frac{\partial F_{n-1}}{\partial T}\right)\right] d\rho \tag{8.A}$$

It is convenient to define a variable $g = 1/\rho_c^2$, which appears in the exponential term, δ, of the above equations. The integral can be expressed in compact form by integrating the exponential part of the integral term by term as:

$$I_1 = \left[\sum_{n=2}^{9} \frac{\rho^{n-1}}{n-1}\left(F_{n-1} - T\frac{\partial F_{n-1}}{\partial T}\right) - e^{-\delta^2} \sum_{n=10}^{15} \left(F_{n-1} - T\frac{\partial F_{n-1}}{\partial T}\right) \frac{1}{2g^{n-9}} \sum_{m=10}^{n-9} \frac{(n-10)!}{m!} \rho^{2m} g^m\right]_0^\rho \tag{9.A}$$

The inner energy can be calculated from specific enthalpy, pressure and density using Eq.(8). The expression for the specific heat capacity at constant volume contains the integral:

$$I_2 = \int_0^\rho \left[\frac{T}{\rho^2}\left(\frac{\partial^2 p}{\partial T^2}\right)_\rho\right]_T d\rho \tag{10.A}$$

Using Eq.(3.A), the second integral can be solved as:

$$I_2 = \left[\sum_{n=2}^{9} \frac{\rho^{n-1}}{n-1} \frac{\partial^2 F_{n-1}}{\partial T^2} - e^{-\delta^2} \sum_{n=10}^{15} \frac{\partial^2 F_{n-1}}{\partial T^2} \frac{1}{2g^{n-9}} \sum_{m=10}^{n-9} \frac{(n-10)!}{m!} \rho^{2m} g^m\right]_0^\rho \tag{11.A}$$

The heat capacity at constant pressure is calculated from Eqs.(2.A), (4.A) and (13.A). The speed of sound is calculated using the isentropic exponent

$$\gamma = \frac{c_p(\rho, T)}{c_v(\rho, T)} \tag{12.A}$$

and the derivative of the pressure with respect to the density, Eq.(4.A). The expression furthermore contains the integral

$$I_3 = \int_0^\rho \frac{1}{\rho^2}\left[\left(\frac{\partial p}{\partial T}\right)_\rho - R\rho\right]_T d\rho \tag{13.A}$$

Considering that the terms with $n = 1$ is equal to:

$$\frac{1}{\rho^2}\frac{\partial p}{\partial T}(n=1)-\frac{R}{\rho}=0 \tag{14.A}$$

The third integral can be rewritten as:

$$I_3=\left[-\sum_{n=2}^{9}\frac{\rho^{n-1}}{n-1}\frac{\partial F_{n-1}}{\partial T}+e^{-\delta^2}\sum_{n=10}^{15}\frac{\partial F_{n-1}}{\partial T}\frac{1}{2g^{n-9}}\sum_{m=10}^{n-9}\frac{(n-10)!}{m!}\rho^{2m}g^m\right]_0^{\rho} \tag{15.A}$$

Finally, Table 4 resumes the coefficients V_i obeserved in Eq.(12), in which the temperature and pressure at the triple point have been assumed equal to 54.36 K and $1.48\cdot 10^{-4}$ MPa and a critical temperature equal to 154.581 K.

Table 3 Functions F_n of the Modified Benedict-Webb-Rubin equation of state (Eq.(6)).

n	F_n	$\partial F_{n-1}/\partial T$	$\partial^2 F_{n-1}/\partial T^2$
0	RT	R	0
1	$G_1T+G_2T^{0.5}+G_3+G_4/T+G_5/T^2$	$G_1+G_2/2T^{0.5}-G_4/T^2-2G_5/T^3$	$G_2/4T^{1.5}+2G_4/T^3+6G_5/T^4$
2	$G_6T+G_7+G_8/T+G_9/T^2$	$G_6-G_8/T^2-2G_9/T^3$	$2G_8/T^3+6G_9/T^4$
3	$G_1T+G_{11}+G_8/T+G_9/T^2$	$G_{10}T-G_{12}/T^2$	$2G_{12}/T^3$
4	G_{13}	0	0
5	0	$-G_{14}/T^2-2G_{15}/T^3$	$2G_{14}/T^3+6G_{15}/T^4$
6	G_{16}/T	$-G_{16}/T^2$	$2G_{16}/T^3$
7	$G_{17}/T+G_{18}/T^2$	$-G_{17}/T^2-2G_{18}/T^3$	$2G_{17}/T^3+6G_{18}/T^4$
8	G_{19}/T^2	$-2G_{19}/T^3$	$6G_{19}/T^4$
9	$G_{20}/T^2+G_{21}/T^3$	$-2G_{20}/T^3-3G_{21}/T^4$	$6G_{20}/T^3+12G_{21}/T^5$
10	$G_{22}/T^2+G_{23}/T^4$	$-2G_{22}/T^3-4G_{23}/T^5$	$6G_{22}/T^3+20G_{23}/T^6$
11	$G_{24}/T^2+G_{25}/T^3$	$-2G_{24}/T^3-3G_{25}/T^4$	$6G_{24}/T^4+12G_{25}/T^5$
12	$G_{26}/T^2+G_{27}/T^4$	$-2G_{26}/T^3-4G_{29}/T^5$	$6G_{26}/T^4+20G_{27}/T^6$
13	$G_{28}/T^2+G_{29}/T^3$	$-2G_{28}/T^3-3G_{29}/T^4$	$6G_{28}/T^4+12G_{29}/T^5$
14	$G_{30}/T^2+G_{31}/T^3+G_{32}/T^4$	$-2G_{30}/T^3-3G_{31}/T^4-4G_{32}/T^5$	$6G_{30}/T^4+12G_{31}/T^5+20G_{32}/T^6$

Table 4 Coefficients G_i for the MBWR EOS (Table 4) and V_i for Eq.(12).

n	G	V
1	-4.36586E-05	7.568956
2	2.00582E-02	5.004836
3	-4.19791E-01	-2.13746
4	1.87822E+01	0
5	-1.28747E+03	3.454481
6	1.55675E-06	1.514

7	1.34364E-04
8	-2.22842E-01
9	4.76779E+02
10	4.79085E-08
11	2.46261E-04
12	-1.92189E-02
13	-6.97832E-07
14	-6.21415E-05
15	-1.86085E-02
16	2.60979E-06
17	-2.44761E-08
18	1.45774E-05
19	-1.72649E-07
20	-2.38489E+02
21	-2.30181E+04
22	-2.79030E+00
23	9.40058E+03
24	-4.16945E-03
25	2.00850E-01
26	-1.25608E-05
27	-6.40636E-02
28	-2.47558E-09
29	1.34631E-06
30	-1.16150E-11
31	-1.03470E-09
32	2.36594E-08
g	0.0056

Finally, the expressions of the contributions composing the oxygen transport properties are given. For the sake of the reader, Eqs.(13) are reported again.

$$\begin{aligned} \mu &= \mu_0(T) + \mu_1(T)\rho + \mu_2(\rho, T) \\ k &= k_0(T) + k_1(T)\rho + k_2(\rho, T) + \Delta k_c(\rho, T) \end{aligned} \tag{16.A}$$

The terms with subscript *0* are the contributions of the dilute gas.

$$\begin{aligned} \mu_0(T) &= \sum_{n=1}^{9} G_{\mu 0,n}\, T^{(4-i)/3} \\ k_0(T) &= \sum_{n=1}^{9} G_{k0,n}\, T^{(4-i)/3} \end{aligned} \tag{17.A}$$

The terms with subscript *1* represent the contribution to the transport coefficients of the moderately gas dense.

$$\mu_1(T) = G_{\mu1,1} + G_{\mu1,2}\left[G_{\mu1,3} - ln\left(T/G_{\mu1,4}\right)\right]^2$$
$$k_1(T) = G_{k1,1} + G_{k1,2}\left[G_{k1,3} - ln\left(T/G_{k1,4}\right)\right]^2 \quad (18.A)$$

The terms with subscript *2* represent the contribution of the gas dense. The expression has been reported only for viscosity, but the same can be repeated for the thermal conductivity.

$$\mu_2(\rho,T) = exp[F(\rho,T) - G(T)]$$
$$F(\rho,T) = G_{\mu2,1} + G_{\mu2,2}H(\rho) + G_{\mu2,3}\rho^{0.1} + G_{\mu2,4}H(\rho)/T^2 + G_{\mu2,5}\rho^{0.1}/T^{1.5} + G_{\mu2,6}/T + G_{\mu2,7}H(\rho)/T \quad (19.A)$$
$$G(T) = G_{\mu2,1} + G_{\mu2,2}/T$$
$$H(\rho) = \rho^{0.5}\left(\rho - G_{\mu2,8}\right)/G_{\mu2,8}$$

The following expression fully describe the thermal properties behaviour of the oxygen excepting in the zone included in the range $(\rho - \rho_c)/\rho < 0.25$ and $(T - T_c)/T < 0.025$, in which the critical enhancement of the thermal conductivity, Δk_c, can be higher than the sum of the other three terms. For a detailed description about the computation of the thermal critical enhancements, see Ref.[25,27]. The constants involved in the calculation of the transport properties are summarized in Table 5.

Table 5 Coefficients required for the calculation of the oxygen thermal properties.

n	$G_{\mu0}$	G_{k0}	$G_{\mu1}$	G_{k1}	$G_{\mu2}$	G_{k2}
1	-9.7076E+3	-2.0395E+2	0.43526	0.0306	2.40881E+2	-2.15207E+1
2	8.2801E+3	2.4088E+2	-0.20361	0.02785	-1.20142E+2	0
3	-2.4668E+3	-1.2014E+2	1.4	1.12	3.29549E+1	1.67995E+1
4	2.1324E+2	3.2954E+1	100	100	-5.42442	0
5	3.7851E+1	-5.4244			5.47349E-1	-2.99449E+3
6	-1.0487E+1	0.54734			-3.28548E-2	4.73505E+2
7	1.1134	-3.2854E-2			1.07536E-3	0
8	-5.3676E-2	1.0753E-3			-1.46110E-5	1
9	1.0279E-3	-1.4610E-5				

References

[1] T. Shimada, C. Carmicino, A. Karabeyoglu, Hybrid Rocket (Volume II), Aerospace, 9(5) (2022), 233. https://doi.org/10.3390/aerospace9050233

[2] C. Carmicino, Advances in Hybrid Rocket Technology and Related Analysis Methodologies, Aerospace, 6(12) (2019), 128. https://doi.org/10.3390/aerospace6120128

[3] D. Altman, A. Holzman, Overview and History of Hybrid Rocket Propulsion. Fundamentals of Hybrid Rocket Combustion and Propulsion, edited by K. Kuo, M. Chiaverini, AIAA Progress in Astronautics and Aeronautics, 218 (2007), 1–36.

[4] K. Kuo, M. Chiaverini, Challenges of Hybrid Rocket Propulsion in the 21st Century, Fundamentals of Hybrid Rocket Propulsion, edited by M. Chiaverini, and K. Kuo, AIAA Progress in Astronautics and Aeronautics, 218 (2006), 593–638.

[5] A. McDonald, P. Hedman, Erosion of Graphite in Solid Propellant Combustion Gases and Effects on Heat Transfer, AIAA Journal, 3 (7) (1965) 1250–1257. https://doi.org/10.2514/3.3117

[6] R. Acharya, K. Kuo, Effect of Pressure and Propellant Composition on Graphite Rocket Nozzle Erosion Rate, Journal of Propulsion and Power, 23 (6) 2007 1242–1254. https://doi.org/10.2514/1.24011

[7] L. Kamps, S. Hirai, K. Sakurai, T. Viscor, Y. Saito, R. Guan, H. Isochi, N. Adachi, M. Itoh, H. Nagata, Investigation of Graphite Nozzle Erosion in Hybrid Rockets Using Oxygen/High-Density Polyethylene, Journal of Propulsion and Power, 36 (3) (2020) 423–434. https://doi.org/10.2514/1.B37568

[8] L. Kamps, K. Sakurai, K. Ozawa, H. Nagata, Investigation of Graphite Nozzle Erosion in Hybrid Rockets Using N2O/HDPE, AIAA Propulsion and Energy 2019 Forum, Indianapolis, IN, 2019. https://doi.org/10.2514/6.2019-4264

[9] H. G. Price, Cooling of High-Pressure Rocket Thrust Chambers with Liquid Oxygen, Journal of Spacecraft and Rockets 18 (4) (1980) 338-343. https://doi.org/10.2514/3.57826

[10] S. Yuasa, K. Kitagawa, T. Sakurazawa, I. Kumazawa, T., Sakurai, Liquid Oxygen Vaporization Techniques for Swirling-Oxidizer-Flow-Type Hybrid Rocket Engines, International Journal of Energetic Materials and Chemical Propulsion, 10 (2) (2011) 155-168. https://doi.org/10.1615/IntJEnergeticMaterialsChemProp.2012001351

[11] S. D. Eilers, S. Whitmore, Z. Peterson, US Patent No. US2014/0026537A1, 2014.

[12] S. Ito, L. Kamps, S. Yoshimal, H. Nagata, Evaluation of the Thermal Onset of Graphite Nozzle Erosion, AIAA Propulsion and Energy 2020 Forum, Virtual Event, 2020. https://doi.org/10.2514/6.2020-3755

[13] H. Kojima, L. Kamps, Y. Nobuhara, H. Nagata, T. Valembois, C. Cottenot, Progress Towards Graphite Nozzle Cooling for Throat Erosion Suppression, AIAA AVIATION 2022 Forum, Chicago, IL & Virtual, 2022. https://doi.org/10.2514/6.2022-3859

[14] M. Pizzarelli, S. Carapellese, F. Nasuti, A Quasi-2-D Model for the Prediction of the Wall Temperature of Rocket Engine Cooling Channels, Numerical Heat Transfer, Part A: Applications, 60 (1) (2011), 1-24. https://doi.org/10.1080/10407782.2011.578011

[15] M. H. Naraghi, M. Foulon, A Simple Approach for Thermal Analysis of Regenerative Cooling of Rocket Engines, Proceedings of the ASME 2008 International Mechanical Engineering Congress and Exposition. Volume 10: Heat Transfer, Fluid Flows, and Thermal Systems, Parts A, B, and C, Boston, Massachusetts, USA, 2008. pp. 531-538. https://doi.org/10.1115/IMECE2008-67988

[16] C. H. Marchi, F. Laroca, A. F. Carvalho da Silva, J. N. Hinckel, Numerical Solutions of Flows in Rocket Engines with Regenerative Cooling, Numerical Heat Transfer, Part A: Applications, 45(7) (2004) 699-717. https://doi.org/10.1080/10407780490424307.

[17] M. Pizzarelli, F. Nasuti, M. Onofri, Analysis of Curved-Cooling-Channel Flow and Heat Transfer in Rocket Engines, J. Propuls. Power, 27(5) (2011) 1045–1053. https://doi.org/10.2514/1.B34163

[18] J. B. Calvo, K. Hannemann, Numerical Simulation of Liquid Rocket Engine Cooling Channels, 45th AIAA/ASME/SAE/ASEE Joint Propulsion Conference & Exhibit, Denver, Colorado, 2009. https://doi.org/10.2514/6.2009-5302

[19] A. Ulas, E. Boysan, Numerical Analysis of Regenerative Cooling in Liquid Propellant Rocket Engines, Aerospace Science and Technology, 24 (1) (2013) 187-197. https://doi.org/10.1016/j.ast.2011.11.006

[20] L. A. Weber, A Modifued Benedict-Webb-Rubin Equation of State for Gaseous and Liquid Oxygen, NASA Report NBSIR 78-882, Texas, 1978, pp. 1-32.

[21] Anon., Isotropic Graphite: Typical Properties,
https://www.tokaicarbon.co.jp/en/products/fine_carbon/pdf/Isotropic_graphite.pdf

[22] A. I. Lutcov, V. I. Volga, B. K. Dymov, Thermal Conductivity, Electric Resistivity and Specific Heat of Dense Graphite, Carbon, 8 (6) (1970) 753-760. https://doi.org/10.1016/0008-6223(70)90100-4

[23] S. Gordon, B. J. McBride, Computer program of complex chemical equilibrium compositions and applications, NASA Reference Publication 1311, 1994.

[24] G. Su, D. S. Viswanath, Generalized thermodynamic properties of real gases: Part II. Generalized Benedict-Webb-Rubin equation of state for real gases, AIChE Journal, 11 (2) (1965) 205-207. https://doi.org/10.1002/aic.690110207

[25] B. A. Younglove. Thermophysical Properties of Fluids. I. Argon, Ethylene, Parahydrogen, Nitrogen, Nitrogen Trifluoride, and Oxygen, Journal of Physical and Chemical Reference Data, 14 (619) (1985) 1-353. https://doi.org/10.1063/1.555731.

[26] H.D. Baehr, S. Kabelac, Thermodynamik: Grundlagen und technische Anwendungen, 13th edition, Springer Berlin, Heidelberg, 2012, pp. 177-234. https://doi.org/10.1007/978-3-642-24161-1

[27] H. J. M. Hanley, R. D. McCarty, W. M. Haynes, The viscosity and thermal conductivity coefficients for dense gaseous and liquid Argon, Krypton, Xenon, Nitrogen and Oxygen, Journal of Physical and Chemical Reference Data, 3 (1979) 979-1017. https://doi.org/10.1063/1.3253152

[28] F. P. Incropera, D. P. DeWitt, T. L. Bergman, A. S. Lavine, Fundamentals of Heat and Mass Transfer, 6th ed., Wiley, 2002, pp. 137-161.

[29] W. H., Lee, A Pressure Iteration Scheme for Two-Phase Flow Modeling," Multi-Phase Transport Fundamentals, Hemisphere Publishing, Washington, 1980.

[30] Q. D. Le, R. Mereu, G. Besagni, V. Dossena, F. Inzoli, Computational Fluid Dynamics Modeling of Flashing Flow in Convergent-Divergent Nozzle, J. Fluids Eng., 140 (10) (2018), 101102. https://doi.org/10.1115/1.4039908

[31] Y. Liao, D. Lucas, 3D CFD Simulation of Flashing Flows in a Converging-Diverging Nozzle, Nucl. Eng. Des., 292 (2015) 149–163. https://doi.org/10.1016/j.nucengdes.2015.06.015

[32] C. Brennen, Fundamentals of Multiphase Flow, Cambridge University Press., Cambridge, 2005.

[33] B. S. Petukhov, Heat transfer and friction in turbulent pipe flow with variable physical properties, Adv. Heat Transf., 6 (1970) 503-564. https://doi.org/10.1016/S0065-2717(08)70153-9

[34] D. R. H. Beattie, P. B. Whalley, A Simple Two-Phase Frictional Pressure Drop Calculation Method, Int. J. Multiph. Flow, 8 (1982) 83-87. https://doi.org/10.1016/0301-9322(82)90009-X
[35] M. S. Bhatti, R. K. Shah, Turbulent and transition flow convective heat transfer in ducts. In Handbook of Single-Phase Convective Heat Transfer, Wiley, New York, 1987.